Planar liquid jet: Early deformation and atomization cascades

A. Zandian, W. A. Sirignano, and F. Hussain

Citation: Physics of Fluids **29**, 062109 (2017); doi: 10.1063/1.4986790
View online: http://dx.doi.org/10.1063/1.4986790
View Table of Contents: http://aip.scitation.org/toc/phf/29/6
Published by the American Institute of Physics

Planar liquid jet: Early deformation and atomization cascades

A. Zandian,[1,a)] W. A. Sirignano,[1] and F. Hussain[2]
[1]*Department of Mechanical and Aerospace Engineering, University of California, Irvine, California 92697, USA*
[2]*Department of Mechanical Engineering, Texas Tech University, Lubbock, Texas 79409, USA*

(Received 11 February 2017; accepted 5 June 2017; published online 22 June 2017)

The temporal evolution of three-dimensional instabilities on a planar liquid sheet segment is studied using direct numerical simulation, and the level-set and volume-of-fluid methods for the liquid-gas interface tracking. Three atomization cascades are distinguished at early breakup, which are well categorized on a gas Weber number (We_g) versus liquid Reynolds number (Re_l) map. These atomization processes include lobe stretching that occurs at low Re_l and low We_g, hole and bridge formation that occurs at moderate Re_l and high We_g, and lobe corrugation occurring at high Re_l and low We_g. Qualitative comparison between the sizes of the ligaments and droplets that result from each process is presented. A transitional region between the prescribed atomization domains is found. At high Re_l, the transitional boundary is a constant Ohnesorge line defined based on gas *We* and liquid *Re* ($Oh_m \equiv \sqrt{We_g}/Re_l$). At low Re_l, the transitional region follows a hyperbolic line on the We_g–Re_l plot. These atomization processes are qualitatively independent of the jet geometry—seen in both planar and round liquid jets. At a constant density ratio, characteristic times for the hole formation and for the lobe and ligament stretching are different—the former depending on surface tension and the latter on liquid viscosity. In the transitional region, both characteristic times are of the same order. *Published by AIP Publishing.* [http://dx.doi.org/10.1063/1.4986790]

I. INTRODUCTION

Transformation of a bulk liquid into sprays in a gaseous atmosphere, i.e., atomization, is important in numerous industrial, automotive, and aerospace applications. Atomization is encountered in applications such as fuel injection, propulsion and combustion systems, agricultural sprays, and chemical reactors. The initial breakup of a liquid jet is often referred to as primary breakup or primary atomization. A population of larger droplets produced in the primary atomization may be unstable at some critical flow conditions and thus may undergo further disruption into smaller droplets. This process is usually termed as secondary atomization.

In most spray systems, reduction in drop size leads to higher volumetric heat release rates, a wider burning range, and lower exhaust concentrations of pollutant emissions. In other applications, however, small droplets must be avoided because their settling velocity is low and, under certain meteorological conditions, they can drift too far downwind. The development of small disturbances, which eventually lead to disintegration into ligaments and then drops, is also important in determining the shape and penetration of the spray as well as its number density, drop velocity, and drop size as functions of time and space.[1]

While increasing relative gas-liquid velocity has been shown to produce smaller droplets, the mechanism for breakup has not been clearly established. The common notion is that the shear causes spanwise waves to form on the surface of the sheet, and the waves grow and separate from the sheet in the form of ligaments, which then fragment into droplets.[2] There have been several numerical and experimental studies on liquid sheet breakup; however, until recently, none of them have been able to explain the breakup mechanisms and delineate the flow parameters affecting those mechanisms.

A. Analytical studies

In the earlier analytical studies, the disintegration of liquid jets was framed in terms of instabilities, which are well known to be critical in the distortion of the liquid-gas interface and in the formation of ligaments torn from the jet core. Linear studies have shown that there can only exist two modes of unstable waves on the two gas-liquid interfaces in a stationary gas medium, corresponding to the two surface waves oscillating exactly in and out of phase, commonly referred to as the sinuous (antisymmetric) and varicose (symmetric) modes.[3,4] The nonlinear calculations of Rangel and Sirignano[5] indicate the dominance of varicose oscillating modes when the density ratio is of the order of one, while sinuous waves prevail at lower gas densities. The breakup of thin planar liquid sheets due to the nonlinear growth of disturbances was explored by Tharakan *et al.*[6] They studied the effects of flow Weber number ($We \equiv \rho U^2 h/\sigma$) on the size of the ligaments and found that the size and geometry of ligaments formed during breakup vary with *We*, giving rise to thinner ligaments as *We* is increased.

Reitz and Bracco,[7] following the original work of Ohnesorge,[8] identified the operational regimes of a round liquid jet breakup into four distinct regimes. The regimes were separated by straight lines with negative slope on the log-log plot of *We* (or Ohnesorge number $Oh \equiv \sqrt{We}/Re$) versus Reynolds

a)Electronic mail: azandian@uci.edu

number ($Re \equiv \rho UD/\mu$). The first domain at lower values of *We* and *Re* is the Rayleigh capillary mechanism region. Aerodynamic interaction with the gas is not significant. Symmetric distortion occurs with the formation of droplets that have a diameter of the same order as the jet thickness. Next is the first wind-induced region where sinuous oscillations occur still resulting in droplet sizes comparable to the jet thickness. The second wind-induced region results in smaller droplets, while the atomization region at the highest values of *We* and *Re* results in the smallest droplets. As *We* or *Oh* increases, the breakup length tends to decrease. The atomization regime is the domain where the breakup process essentially begins at the orifice exit and is of much broader practical interest but yet far less studied than the other three domains. That atomization domain is the focus of our study here.

None of the studies above addressed the 3D nonlinear behavior, and thus, none addressed the key behavior for high *Re* and high *We* flows—a form of transitional turbulence in the range of interest in practical atomizers.

B. Experimental studies

The transient behavior of liquid injection has been the subject of numerous experimental studies for planar liquid sheets.[2,9–12] Typically, these experiments are conducted at atmospheric pressure with very low gas-to-liquid density ratios. Fraser *et al.*[9] defined three modes of sheet disintegration, described as rim, wave, and perforated-sheet disintegration. Stapper *et al.*[2] suggested two breakup regimes of a liquid sheet: cellular breakup at high gas-to-liquid relative velocities and stretched ligament breakup at lower relative velocities. The relative strength of the spanwise and streamwise vortical waves in the sheet was a controlling factor in the breakup mechanism. Their study revealed that the relative gas-liquid velocity is a primary factor in the ligament formation and breakup. The breakup is a complex three-dimensional interaction of spanwise and streamwise waves, between which are stretched thin film membranes, and an increase in relative velocity leads to further stretching of both the liquid membranes and streamwise ligaments, both leading to smaller droplets. They also showed that the variation in the liquid properties did not alter the general character of the two breakup mechanisms; however, it had a pronounced effect on the time and length scales. Most of their study was focused on relatively low *Re* (e.g., 100–3000) and low *We* [e.g., $O(10^1$–$10^3)$].

Hoyt and Taylor[13] in their study of waves on round water jets observed that the mechanism of jet breakup was related to the relative air velocity and hence to the drag on the perturbed jet. Thus, they concluded that the mechanism of jet breakup is a form of drag on the helical components of the jet, since jets discharging into a surrounding gas moving at the same speed as the jet remain relatively stable. The *Re* based on jet speed and diameter was about 10^5 in their study.

Planar laser-induced fluorescence (PLIF) was used by Lozano and Barreras[10] to visualize the air-flow in the near field of an air-blasted breaking water sheet. They used the air-water momentum ratio to characterize different breakup regimes. Their two-phase flow visualization revealed detachment of the air boundary layer over the air-water interface behind the zones of strong curvature and identified the pressure field induced by these vortices as a cause of the enhanced sheet flapping and instability growth. Their experiments were conducted at fairly high *Re* of order 10^4 and low *We* of order 10^3. Park *et al.*[11] studied the cellular breakup mechanism for a planar liquid sheet with assisting air streams from an air-blast nozzle. The measured average size of cellular structures and thus the dominant wavelength were found to be proportional to the inverse square of the relative velocity between air and liquid.

Wahono *et al.*[12] used high-speed imaging to qualitatively visualize the structure of the annular spray at low *We* ($\sim 10^2$) and relatively low *Re* ($\sim 10^3$). Their particular interest was the evolution of the spray into a ligament structure during the primary breakup and the role of the outer air stream. They showed that thicker and longer ligaments are formed at higher *Re*'s, which is attributed to higher liquid momentum.

Even though several types of breakup mechanisms and the corresponding ligament and droplet sizes have been introduced by several experimentalists, they have not clearly identified the domain in which these breakups occur. Moreover, many of the studies focused on very low *Re* and *We*, which is far from the domain of interest in most applications. Generally, experiments have not been able to reveal the details of the smaller structures that develop during cascade of atomization (with the work of Marmottant and Villermaux[14] as an exception) and only the quality of the developed ligaments and droplets at the end of the breakup has been discussed. In this regard, the numerical simulations have proven to be a much better tool to investigate the mechanisms of the primary atomization.

C. Computational studies

A list of computational studies on planar and round liquid jets is given in Table I. The range of each nondimensional parameter and the type of the study are also denoted in this table. In one of the earliest numerical studies on the liquid jet instability, Lozano *et al.*[15] implemented a three-dimensional Lagrangian code based on vortex dynamics to track the air-liquid interface, treated as inviscid vortex sheets. Using the vortex dynamics and altering the initial perturbation orientation with respect to the flow direction, they were able to propose mechanisms for generation of spanwise and streamwise ligaments.

Scardovelli and Zaleski[16] analyzed the response to spanwise perturbations of the two-dimensional base flow in their three-dimensional simulations at very low *Re* and *We*. They were able to distinguish two scenarios by which three-dimensional flows set in. For small three-dimensional perturbations, the simulation remains two-dimensional until the sheet breaks up and a cylinder with spanwise axis pinches off. Subsequently, the capillary instability gives a three-dimensional structure to the flow. In contrast, for higher three-dimensional perturbations, the rim-like edge concentrates in protruding ligaments that will be subject to the capillary instability. However, the unstable cylinder is now streamwise oriented. The formation of streamwise ligaments is also observed in real experiments on shear layers.[14]

TABLE I. List of computational studies on liquid jets, their parameters range, jet configuration, and type of study.

Study	Configuration	Type of study	*Re*	*We*	Density ratio	Viscosity ratio
Lozano *et al.*[15]	Planar	Temporal	∞	$O(10^5)$	Not reported	NA
Scardovelli and Zaleski[16]	Planar	Temporal	1 000	300–2 000	0.1	Not reported
Desjardins and Pitsch[17]	Planar	Temporal	2 000–3 000	500–2 000	0.025	0.025
Shinjo and Umemura[18]	Round	Spatial	1 000–3 000	3 000–30 000	0.04	0.007
Herrmann[19]	Round	Spatial	5 000	17 000	0.03	0.01
Jarrahbashi *et al.*[20,21]	Round	Temporal	320–16 000	2 000–230 000	0.05–0.9	0.002–0.035
Zandian *et al.*[22]	Planar	Temporal	500–10 000	3 000–72 000	0.5–0.9	0.0001–0.01

A detailed numerical investigation of turbulent liquid jets in quiescent air at low gas-to-liquid density ratio was conducted by Desjardins and Pitsch[17] to identify the key atomization mechanisms and to analyze the effects of the jet *Re* and *We*. Their work was limited to very low *We* compared to the range of interest for common liquid fuels and high-pressure operations. They found that liquid turbulence plays an important role in the generation of the first droplets, while the Kelvin-Helmholtz (KH) instabilities are not visible at early times. Several detailed atomization mechanisms have also been identified by them, such as bubble formation through sweep-ejection events and ligament generation due to bubble bursting or droplet collision. The instantaneous liquid-gas interface in their computations showed some hole formation near the tips of a few of the liquid sheets expelled from the planar jet core, tearing of those sheets, and formation of the ligaments due to tearing for *Re* and *We* equal to 2000 and 1000, respectively. They did not explain the mechanisms of hole formation though.

Computational studies of Shinjo and Umemura[18] on the primary atomization of a round liquid jet injected into high-pressure still air, at higher *We* than that of Desjardins and Pitsch,[17] indicated ligament formation from the development of holes in the liquid crests. They showed that disturbances propagate upstream from the liquid jet tip through vortices and droplet re-collision. They claimed that collision of the droplets—broken from the ligaments formed at the back of the mushroom-shaped cap—with the liquid jet core formed holes on the lobes. When the lobe surface area increased and its rims became thicker, the lobe surface punctured to form two or three ligaments as the hole extended to the tip of the lobe.

Lobe perforation leading to ligament formation similar to the mechanism observed by Shinjo and Umemura[18] was also observed by Jarrahbashi and Sirignano[20] for larger gas-to-liquid density ratios. However, unlike the claims of Shinjo and Umemura,[18] holes formed on the lobes even before the ligaments form and break up into droplets. Therefore, most probably, droplet collision with the liquid jet core is not the only factor, nor even the major factor, promoting hole formation.[21] Computational simulations of round liquid jets by Herrmann[19] showed the disintegration of the liquid core to ligaments and droplets and also predicted the droplet sizes. However, ligament formation mechanisms were not addressed.

The liquid jet from a round orifice during the transient start-up and steady mass flux periods of a high-pressure injector was studied via Navier-Stokes and level-set (LS) computations by Jarrahbashi and Sirignano[20] and Jarrahbashi *et al.*[21] A wide range of density ratio, *Re*, and *We* were covered. The role of vorticity dynamics was examined via post-processing. They show that the three-dimensional instability starts as a result of the appearance of counter-rotating pairs of streamwise vortices in between two consecutive vortex rings, which are actually hairpin vortices wrapped around the vortex rings, and produce the first lobes. They also found that, for low gas-to-liquid density ratios, ligaments mostly form due to elongation of the lobes themselves; however, most of the ligaments form as a result of hole tearing at higher density ratios.

In the latest numerical analysis by Zandian *et al.*,[22] various breakup patterns are identified at different flow regimes for a wide range of viscosity ratio, *Re*, and *We* similar to the range covered by Jarrahbashi and Sirignano[20] and high density ratios of a thin liquid sheet. Two distinct mechanisms were proposed regarding breakup of the liquid lobes into droplets: hole formation and expansion, and formation of ligaments due to stretching of the lobes, which happen at low/medium and high *Re*'s, respectively. The cascade of structures and their cause was explained from a vorticity dynamics perspective.

D. Objectives

The goals of this research are to detail and explain (i) cascade of structures on the liquid surface with time, including lobe, ligament, and droplet formations; (ii) character of the breakup mechanisms at different flow conditions; (iii) the effects of density ratio, viscosity ratio, and sheet thickness on the liquid sheet breakup; and (iv) proper definition of the time scale of each of the breakup mechanisms, which would help predict the dominant mechanism at different flow conditions.

In Sec. II, the numerical methods and the most important flow parameters involved in this study are presented. The results are presented in Sec. III. The different breakup mechanisms that have been observed are introduced and the classification of the domain into different breakup categories is defined in Sec. III A. Also, the effects of *Re* and *We*, density ratio, viscosity ratios, and the sheet thickness are analyzed in Secs. III B–III E, respectively. A quick look at the effects of density ratio on the streamwise vorticity production is presented in Sec. III F, and the comparison between the planar and the round jet results is discussed in Sec. III G. In Sec. III H,

the time scales of the breakup mechanisms are studied. The most important findings of this study are summarized in Sec. IV.

II. NUMERICAL MODELING

A. Governing equations

The governing equations are the continuity, momentum, and level-set/volume-of-fluid (VoF) equations. Since both the gas and the liquid are incompressible, the continuity equation is

$$\nabla \cdot \mathbf{u} = 0, \tag{1}$$

where $\mathbf{u}$ is the velocity vector. The momentum equation, including the viscous diffusion and surface tension forces and neglecting the gravitational force, is

$$\frac{\partial(\rho \mathbf{u})}{\partial t} + \nabla \cdot (\rho \mathbf{u}\mathbf{u}) = -\nabla p + \nabla \cdot (2\mu \mathbf{D}) - \sigma \kappa \delta(d)\mathbf{n}, \tag{2}$$

where p, ρ, and μ are the pressure, density, and dynamic viscosity of the fluid, respectively. $\mathbf{D}$ is the rate of deformation tensor,

$$\mathbf{D} = \frac{1}{2}\left[(\nabla \mathbf{u}) + (\nabla \mathbf{u})^T\right]. \tag{3}$$

The last term in Eq. (2) is the surface tension force per unit volume, $\mathbf{F} = -\sigma\kappa\delta(d)\mathbf{n}$, where σ is the surface tension coefficient, κ is the surface curvature, $\delta(d)$ is the Dirac delta function, d is the distance from the interface, and $\mathbf{n}$ is the unit vector normal to the liquid-gas interface.

The level-set function ϕ is defined as a smooth distance function, which enables evaluation of the density, viscosity, and surface tension at any distance from the interface on either gas or liquid zone (this method was developed by Osher and his co-workers[23–25]). In this algorithm, the interface Γ is the zero level set of ϕ,

$$\Gamma = \{\mathbf{x} \,|\, \phi(\mathbf{x}, t) = 0\}.$$

We take $\phi < 0$ in the liquid region and $\phi > 0$ in the gas region. $\mathbf{u}$ is continuous across the interface. Since the interface moves with the fluid particles, the evolution of ϕ is then given by

$$\frac{\partial \phi}{\partial t} + \mathbf{u} \cdot \nabla \phi = 0, \tag{4}$$

which is called the level-set equation. If the initial distribution of the level set is a signed distance function, after a finite time of being convected by a nonuniform velocity field, it will not remain a distance function. Therefore, the level-set function should be re-initialized in such a way that it will be a distance function, without changing the zero level set (position of the interface). This is achieved by solving the following ordinary differential equation (Sussman *et al.*[24]):

$$\frac{\partial d}{\partial \tau} = \text{sign}(\phi)(1 - |\nabla d|), \tag{5}$$

with initial condition

$$d(\mathbf{x}, 0) = \phi_0(\mathbf{x}),$$

where τ is a pseudo time. The steady solutions of Eq. (5) are distance functions. Furthermore, since sign(0) = 0, then $d(\mathbf{x}, t)$ has the same zero level set as $\phi(\mathbf{x})$.

The governing equation for the fluid velocity $\mathbf{u}$, i.e., Eq. (2), can be written as a single equation containing both liquid and gas properties,

$$\rho(\phi)\frac{D\mathbf{u}}{Dt} = -\nabla p + \nabla \cdot (2\mu(\phi)\mathbf{D}) - \sigma\kappa(\phi)\delta(\phi)\mathbf{n}. \tag{6}$$

Since the density and viscosity are constant in each fluid, they take on two different values depending on the sign of ϕ, and we can write

$$\rho(\phi) = \rho_l + (\rho_g - \rho_l)H(\phi), \tag{7}$$

and

$$\mu(\phi) = \mu_l + (\mu_g - \mu_l)H(\phi), \tag{8}$$

where $H(\phi)$ is a smoothed Heaviside function and the subscripts g and l refer to the gas and liquid, respectively.

At low density ratios, we use a transport equation similar to the level-set equation, i.e., Eq. (4), for the volume fraction f, also called the volume-of-fluid (VoF) variable, in order to describe the temporal and spatial evolution of the two-phase flow,[26]

$$\frac{\partial f}{\partial t} + \mathbf{u} \cdot \nabla f = 0, \tag{9}$$

where the VoF-variable f represents the volume of (liquid phase) fluid fraction as follows:

$$f(\mathbf{x}, t) = \begin{cases} 0, & \text{outside of liquid phase,} \\ 0 < f < 1, & \text{at the interface,} \\ 1, & \text{inside the liquid phase.} \end{cases} \tag{10}$$

The normal direction of the fluid interface is found where the value of f changes most rapidly. With this method, the free-surface is not defined sharply; instead, it is distributed over the height of the cell. Thus, in order to be accurate, local grid refinements have to be done for the cells with $0 < f < 1$. Since fluid properties are required every time step in order to solve the Navier-Stokes equations, the density and viscosity change continuously based on Eqs. (7) and (8). However, in these equations, the argument of the Heaviside function is replaced by f, in the VoF method.

The formulation for the fully conservative momentum convection and volume fraction transport, the momentum diffusion, and the surface tension are treated explicitly. To ensure a sharp interface of all flow discontinuities and to suppress numerical dissipation of the liquid phase, the interface is reconstructed at each time step by the PLIC (piecewise linear interface calculation) method proposed by Rider and Kothe.[27] The liquid phase is transported on the basis of its reconstructed distribution. The capillary effects in the momentum equations are represented by a capillary tensor as introduced by Scardovelli and Zaleski.[16]

B. Flow configuration

The computational domain, shown in Fig. 1, consists of a cube, which is discretized into uniform-sized cells. The liquid segment, which is a sheet of thickness h ($h = 50\ \mu$m for the thin sheet and 200 μm for the thick sheet in this study), is centered at the middle of the box and is stationary at the beginning. The domain size in terms of the sheet thickness h is $16h \times 10h \times 10h$, in the x, y, and z directions, respectively, for the thin

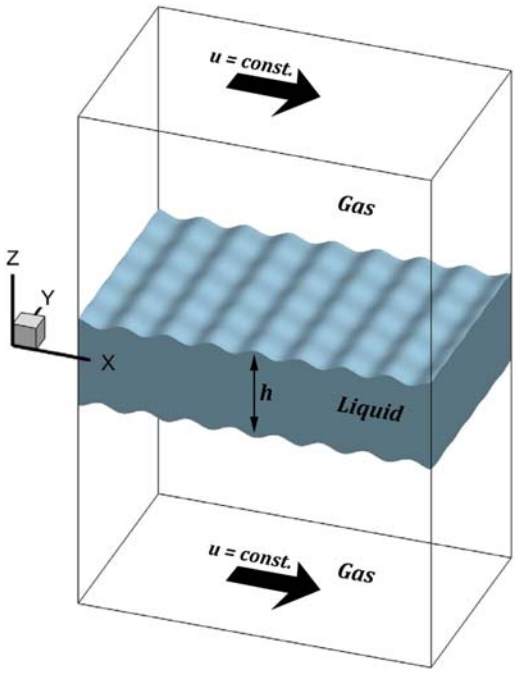

FIG. 1. The 3D liquid segment computational domain with the initial liquid and gas zones.

sheet, and $4h \times 4h \times 8h$ for the thick sheet. The liquid segment is surrounded by the gas zones on top and bottom. The gas moves in the positive (streamwise) x-direction with a constant velocity ($U = 100$ m/s) at the top and bottom boundaries, and its velocity diminishes to the interface velocity with a boundary layer thickness obtained from the 2D simulations. In the liquid, the velocity decays to zero at the center of the sheet with a hyperbolic tangent profile. For more detailed description of the initial conditions, see Fig. 12 in the work of Zandian *et al.*[22]

The flow-field is theoretically infinite in each direction (albeit limited for computation). The flow is initially laminar and vorticity can only be generated in the interfacial shear region. The liquid-gas interface is initially perturbed symmetrically on both sides with a sinusoidal profile and predefined wavelength and amplitude obtained from the 2D full-jet simulations (see Ref. 22). Both streamwise (x-direction) and spanwise (y-direction) perturbations are considered in this study. Periodic boundary conditions for all components of velocity as well as the level-set/VoF variable are imposed on the four sides of the computational domain, i.e., the x and y planes.

The most important dimensionless groups in this study are the Reynolds number (Re), the Weber number (We), and the gas-to-liquid density ratio ($\hat{\rho}$) and viscosity ratio ($\hat{\mu}$), as defined below. The initial wavelength-to-sheet-thickness ratio (Λ) is also an important parameter that defines the relative size of the initial perturbations,

$$Re = \frac{\rho_l U h}{\mu_l}, \; We = \frac{\rho_l U^2 h}{\sigma}, \tag{11a}$$

$$\hat{\rho} = \frac{\rho_g}{\rho_l}, \; \hat{\mu} = \frac{\mu_g}{\mu_l}, \; \Lambda = \frac{\lambda}{h}. \tag{11b}$$

The sheet thickness h is considered as the characteristic length and the velocity of the far field gas U as the characteristic velocity. Theoretically, if the flow field is infinite in the streamwise direction (as in our study), a Galilean transformation shows that only the relative velocity between the two streams is consequential. Spatially developing flow fields, however, are at most semi-infinite so that both velocities at the entry into the domain and their ratio are important. A wide range of Re and We numbers at high and low density ratios is covered in this research.

C. Numerical methods

Direct numerical simulation is done by using an unsteady three-dimensional finite-volume solver to solve the Navier-Stokes equations for the planar incompressible liquid sheet segment (initially stagnant), which is subject to instabilities due to a gas stream that flows past it on both sides. The level-set (LS) and volume-of-fluid (VoF) methods are used for liquid-gas interface tracking. The temporal deformation of the liquid-gas interface is predicted, resulting in three-dimensional instabilities, which can lead to ligament formation and sheet breakup. The original code containing the LS subroutines was developed and applied by Dabiri *et al.*,[28] and later by Jarrahbashi and Sirignano,[20] Jarrahbashi *et al.*,[21] and Zandian *et al.*[22] Because of the weakness of the level-set method in mass conservation at low density ratios, the VoF method is used at low gas densities.

A uniform staggered grid is used with the mesh size of 2.5 μm and a time step of 5 ns—a finer grid resolution of 1.5 μm is used for the higher We (=230 000). Third-order accurate QUICK scheme is used for spatial discretization and the Crank-Nicolson scheme for time marching. The velocity-pressure coupling is established using the SIMPLE algorithm. The initial velocity profile and some other initial estimations (initial surface perturbation wavelength) are obtained from a 2D planar full-jet simulation, with the same schemes and methodology as those of Zandian *et al.*[22]

The grid independency tests were performed previously by Zandian *et al.*[22] and Jarrahbashi *et al.*[20,21] They showed that the errors in the size of the ligaments, penetration length of the liquid jet, and the magnitude of the velocity computed using different mesh resolutions were within an acceptable range. The effects of the mesh size, the thickness of the fuzzy zone between the two phases, where properties have large gradients to approximate the discontinuities, and mass conservation of the level-set method have also been addressed. The domain-size independency was also checked in both streamwise and spanwise directions to ensure that the resolved wavelengths were not affected by the domain length or width. The normal dimension of the domain was chosen such that the top and bottom boundaries remain far from the interface at all times; hence the surface deformation is not directly affected by the boundary conditions. In addition, accuracy tests and validation with experiments and other numerical approaches were performed previously[20,28] and will not be repeated here.

III. RESULTS AND DISCUSSION

A. Atomization classification

Three different processes for liquid surface deformation and breakup are identified—each applying in a different

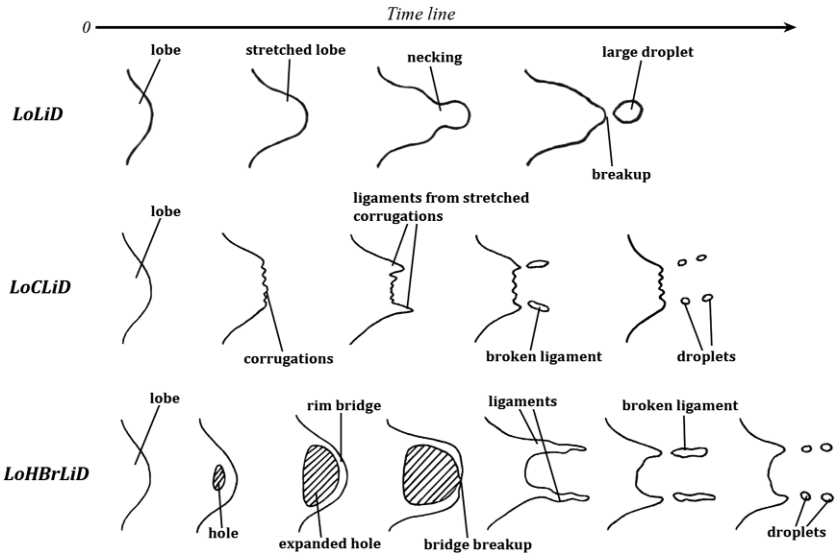

FIG. 2. Cascade of structures for the *LoLiD* (top), *LoC LiD* (center), and *LoH Br LiD* (bottom) processes; sketch showing the top view of a liquid lobe undergoing these processes. The gas flows on top of these structures from left to right, and time increases to the right.

domain of the liquid Reynolds (Re_l) and Weber (We_l) numbers. The liquid structures seen in each cascade process are sketched in Fig. 2, where the evolution of a liquid lobe is shown from a top view of Fig. 1, i.e., in the negative z-direction. At high Re_l, these breakup characteristics change based on the Ohnesorge number ($Oh = \sqrt{We_l}/Re_l$). At relatively high Re_l (>2500), two of these mechanisms were observed in our computations as follows: (i) at high Oh and high Re_l, the lobes become thin and puncture, creating holes and bridges. The bridges break as the perforation expands and create ligaments. The ligaments then stretch and break up into droplets by capillary action. This domain is indicated as Atomization Domain II, and its process is hereafter called *LoHBrLiD*, based on the cascade or sequence of the structures seen in this domain, e.g., $Lo \equiv$ Lobe, $H \equiv$ Hole, $Br \equiv$ Bridge, $Li \equiv$ Ligament, and $D \equiv$ Droplet. (ii) At low Oh and high Re_l, lobe perforations are not seen at early times; instead, many corrugations form on the lobe front edge and stretch into ligaments. This process occurs in Atomization Domain III and is called *LoC LiD* ($C \equiv$ Corrugation). This cascade process results in ligaments and droplets without the hole and bridge formation steps in between. The ligaments formed in this process are typically shorter and thinner compared to the long and thick ligaments in the former mechanism. The third mechanism follows a *LoLiD* process and occurs in Atomization Domain I, at low Re_l and low We_l, but with some difference in the details from the *LoC LiD* process. The main difference between the two ligament formation mechanisms at high and low Re_l's is that, at higher Re_l, the lobes become corrugated before stretching, and then the corrugations are stretched into ligaments. Thereby, each lobe may produce multiple ligaments, which are typically thinner and shorter than those at lower Re_l. At low Re_l, on the other hand, because of the higher viscosity, the entire lobe stretches into one thick and usually long ligament. The droplets produced in Domain I at low Re_l are fairly large compared to those of Domain III.

More cases were computed near the border of Domains I/III and II, showing that there is a transitional region in which both lobe/ligament stretching and hole formation mechanisms are seen simultaneously. Based on the cases that have been run, and also from the physics of the problem, it seems that the liquid viscosity, and thus the liquid Re, has the most significant effect on the stretching characteristic, while the surface tension and the gas inertia, thus the gas We, have an important role in the hole formation. Pursuant to this notion, different breakup characteristic domains are defined in the parameter space of the liquid Reynolds (Re_l) and gas Weber (We_g) numbers. Using We_g allows embedding the effects of density ratio in the classification. Thus, a generic diagram is produced that represents all density ratios on a single plot, which identifies the three atomization sub-domains defined above, shown in Fig. 3.

The high and low density-ratio cases that overlap in our diagram are indicated in Fig. 3. The transitional region at low

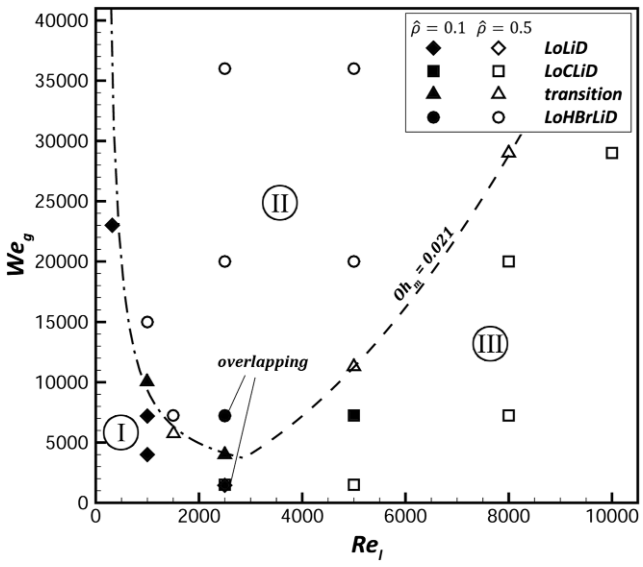

FIG. 3. The breakup characteristics based on We_g and Re_l, showing the *LoLiD* mechanism (Atomization Domain I) denoted by diamonds, the *LoH Br LiD* mechanism (Atomization Domain II) denoted by circles, the *LoC LiD* mechanism (Atomization Domain III) denoted by squares, and the transitional region denoted by triangles. The cases with density ratio of 0.1 ($\hat{\rho} = 0.1$) are shaded. The $\hat{\rho} = 0.1$ and $\hat{\rho} = 0.5$ cases that overlap at the same point on this diagram are noted. – · – · –, transitional boundary at low Re_l; and – – –, transitional boundary at high Re_l.

Re_l follows a hyperbolic relation, i.e., $We_g = A/Re_l$, denoted by dashed-dotted line, while at high Re_l limit, it follows a parabolic curve, i.e., $We_g = B^2 Re_l^2$, denoted by dashed line. The constant B is a critical value of the product of Oh and the square root of density ratio and hereafter is defined as a modified Oh, i.e., Oh_m. Oh_m is defined using the gas We and liquid Re, i.e., $Oh_m \equiv \sqrt{We_g}/Re_l = \sqrt{\hat{\rho}} \times Oh$. The critical Oh_m at the boundary for high Re_l then becomes $Oh_{m_c} = B \approx 0.021$.

Thus, two parameters, A and B, are used to define the domain boundary. At high Re_l, we have parameter B. The parameter B involves four forces and is the ratio of the product of liquid viscous force and square root of gas inertia to the product of liquid inertia and square root of surface tension force. Asymptotically, the domain boundary goes to constant B (constant Oh_m) at high Re_l. The second parameter is $A \sim We_g \times Re_l$. It is the ratio of the product of gas inertia and liquid inertia to the product of surface tension force and liquid viscous force. Again, four forces are involved. At low Re_l, the domain boundary approaches $A = const.$ as an asymptote.

Clearly, four forces are involved in different ways at the two (left and right) boundaries. The connection between vortex dynamics and surface dynamics near the right (high Re_l) and left (low Re_l) boundaries have been examined by Zandian *et al.*,[29] explaining the liquid structure cascade processes in each domain. The two borderlines can be combined into a single function with some extra constants for a better fit as follows:

$$We_g = \frac{A}{Re_l + \epsilon} + B^2 Re_l^2 + C, \tag{12}$$

where A, B, and C are empirical constants and ϵ is a small parameter for better curve fitting. As Re_l gets very large, we would retain the parabolic function (second term) with the constant B being the product of critical Oh and $\sqrt{\hat{\rho}}$. In the limit where Re_l gets very small, the hyperbolic function (first term) dominates and gives the asymptote.

The We_g and Re_l variables in Eq. (12) can be normalized by their values at the minimum point on the parabola-like boundary of Fig. 3 ($Re_r = 2500$ and $We_r = 4900$). The new minimum point then becomes $We_n = 1$ and $Re_n = 1$, and the coefficients a, b, and c would become of order unity (the subscript n means that the variables have been normalized). The normalized boundary equation then becomes

$$\frac{We_g}{We_r} = \frac{a}{\frac{Re_l}{Re_r} + \epsilon} + b^2 \left(\frac{Re_l}{Re_r} \right)^2 + c, \tag{13}$$

with the normalized coefficients that best fit our transitional boundary

$$a = 0.816, \quad b = 0.75, \quad c = -0.4, \quad \epsilon = -0.04\,. \tag{14}$$

Based on these results, there are different characteristic times for formation of holes and stretching of lobes/ligaments. At the same Re_l, as surface tension increases (decreasing We_g), the characteristic time for hole formation becomes larger, hence delaying the hole formation. Thereby, most of the earlier ligaments are formed due to direct stretching of the lobes and corrugations, while hole formation is hindered (Domain III). On the other hand, as liquid viscosity increases (decreasing Re_l and increasing Oh_m), while keeping We_g the same, the characteristic time for ligament stretching gets larger if Re_l is high. In this case, the hole formation prevails compared to the ligament stretching, resulting in more holes on the lobes surface (Domain II). At very low Re_l, the characteristic time of the hole formation is also influenced by the liquid viscosity and gets larger with decreasing Re_l; thus, the breakup mechanism switches back to direct stretching as Re_l is sufficiently lowered (Domain I).

In conclusion, the transitional region is not monotonic on a We_g vs. Re_l diagram and has a minimum value around $Re_l \approx 2500$. Thus, if We_g is less than a certain value (around $We_g = 5000$), the ligament stretching mechanism will always prevail regardless of Re_l. At higher We_g (>5000), the *LoLiD* and *LoC LiD* processes are dominant in Domains I and III at very low and very high Re_l's, respectively, but there exists a Domain II between them where hole formation prevails.

The atomization processes are functions of Re_l and We_g only. The following sub-sections will show that the qualitative behavior is not much affected by the viscosity ratio (thus the gas Re); the influence of density ratio appears only through We_g, and the effect of sheet thickness appears only through Re_l and We_g.

B. Reynolds and Weber numbers effects

As discussed above, Re_l and We_g are the main parameters affecting the breakup mechanism. The atomization regime is divided into three sub-domains, each having a distinct atomization cascade during their early breakup: (i) *LoLiD* process at low Re_l and low We_g in Atomization Domain I; (ii) *LoH Br LiD* process at high We_g and moderate Re_l in Domain II; and (iii) *LoC LiD* process at high Re_l and low We_g in Domain III, which involves corrugation formation. There is also a transitional region between Domains I/III and II, where each cascade process occurs locally. In this section, these processes and the cascade of structures are discussed in detail.

Four cases are presented in this section for a thick liquid sheet ($\lambda/h = 0.5$). Each of these cases was chosen from a separate domain identified in Fig. 3—one from Domain II at $Re_l = 2500$ and $We_g = 7250$, one from Domain III at high $Re_l = 10\,000$ and low $We_g = 29\,000$, one from Domain I at very low $Re_l = 320$ and low $We_g = 23\,000$, and the last one from the transitional region with $Re_l = 5000$ and $We_g = 11\,300$. Except for the third case which is at a low density ratio of 0.1, the rest of the cases are at $\hat{\rho} = 0.5$. The following figures show the atomization cascades occurring in each domain. In all of the figures, the gas flows over the liquid sheet in the positive x-direction, from left to right.

Figure 4 shows the liquid surface deformation in a period between 86 μs and 94 μs, for a thick sheet with $Re_l = 2500$ and $We_g = 7250$ ($Oh_m \approx 0.034$). Based on the criterion that was introduced in Fig. 3, this case falls into Atomization Domain II with the *LoH Br LiD* cascade process. The lobes puncture to make holes at 86 μs. The holes expand and create bridges, which later break up and create one or two ligaments at 88 μs, depending on the breakup location. The ligaments stretch (at 92 μs) and break into droplets at later times (94 μs). The final ligaments of this domain are comparatively long and thick.

Figure 5 shows the surface deformation for a thick liquid sheet with high $Re_l = 10\,000$ and $We_g = 29\,000$ ($Oh_m \approx 0.017$)

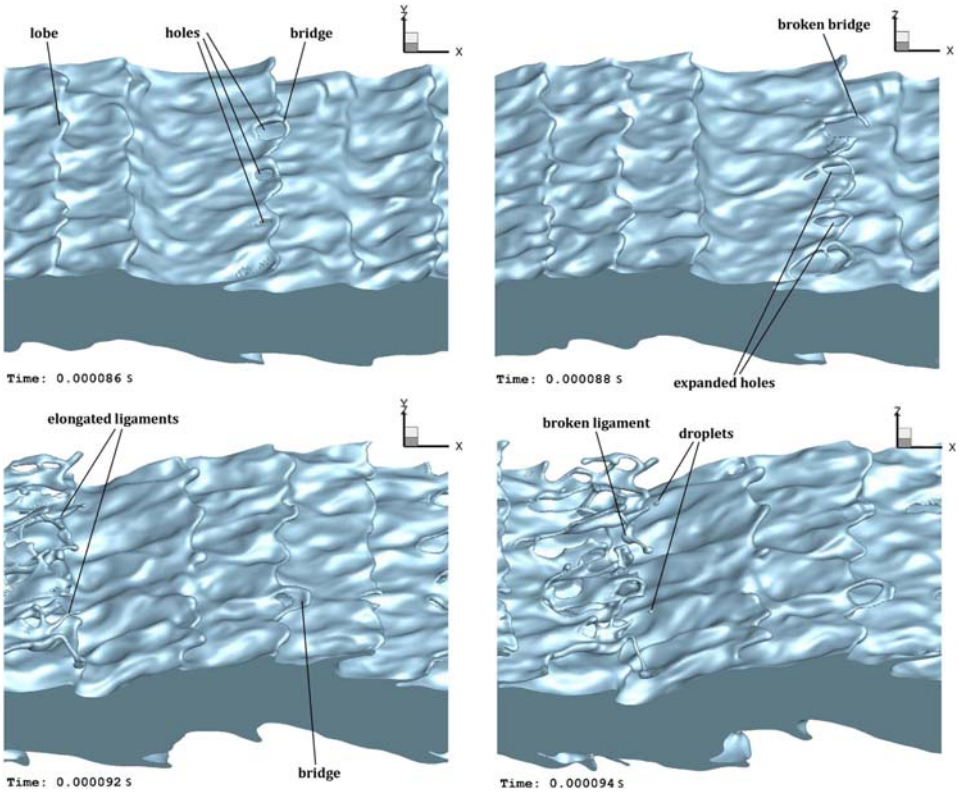

FIG. 4. Liquid surface deformation for the *LoH Br LiD* process (Atomization Domain II) at different times, for a thick liquid sheet $h = 200\ \mu$m; $Re_l = 2500$, $We_g = 7250$, $\hat{\rho} = 0.5$, and $\hat{\mu} = 0.0066$ ($Oh_m = 0.034$). The time is indicated at the left bottom corner of each frame.

during 80–86 μs. The liquid sheet atomization does not involve hole and bridge formation in this domain (III) and follows the *LoC LiD* process. The lobe edges are not as smooth as in the previous case and several corrugations are formed on the edge of the lobes at 82 μs. The corrugations stretch into ligaments later. In this domain, each lobe may produce multiple ligaments. The ligaments look thinner and shorter, compared to the earlier case. These breakup

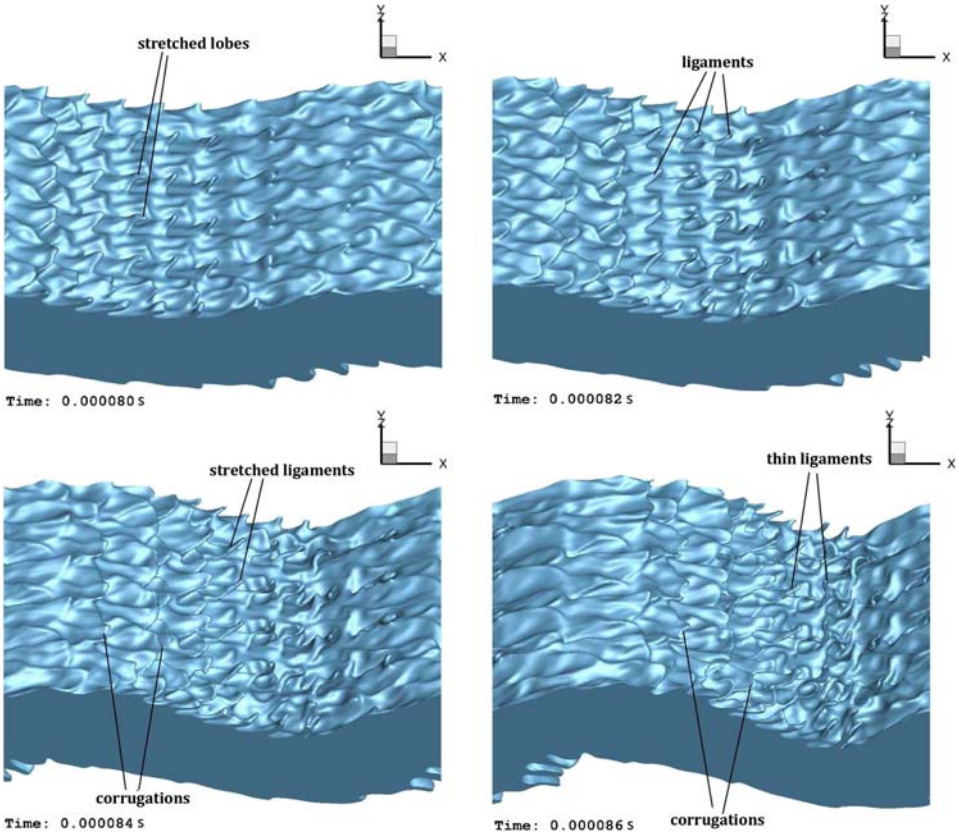

FIG. 5. Liquid surface deformation for the *LoC LiD* process at high Re_l (Atomization Domain III) at different times, for a thick liquid sheet $h = 200\ \mu$m; $Re_l = 10\,000$, $We_g = 29\,000$, $\hat{\rho} = 0.5$, and $\hat{\mu} = 0.0066$ ($Oh_m = 0.017$). The time is indicated at the left bottom corner of each frame.

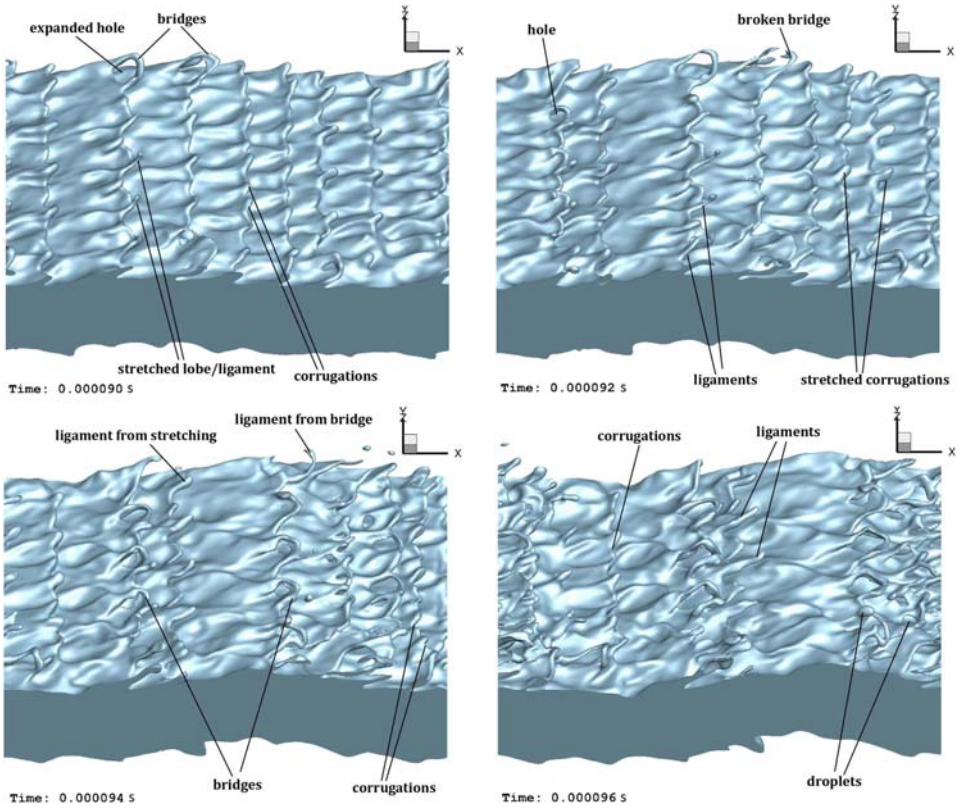

FIG. 6. Liquid surface in the transitional region at different times, for a thick liquid sheet $h = 200\ \mu$m; $Re_l = 5000$, $We_g = 11\,300$, $\hat{\rho} = 0.5$, and $\hat{\mu} = 0.0066$ ($Oh_m = 0.021$). The time is indicated at the left bottom corner of each frame.

characteristics agree with the classification introduced in Fig. 3.

Figure 6 shows the atomization of a thick liquid sheet in the transitional region. In this case, $Re_l = 5000$ and $We_g = 11\,300$, resulting in $Oh_m = 0.021$, placing this case in the transitional category. Both hole formation and lobe stretching mechanisms are seen simultaneously at different locations on the liquid surface. Thus, the characteristic times of these mechanisms are comparable. Which mechanism prevails depends on the balance between the surface tension and viscous forces. If the surface tension force dominates, the hole formation is hindered and lobes are stretched instead. On the other hand, if the viscous effects are dominant, it is more difficult to stretch the lobes into ligaments, and more holes and bridges are formed instead. Since the characteristic times of these two effects are of the same order in the transitional zone, the prevailing mechanism varies locally. Thus, both processes occur at different parts of the sheet surface. The ligaments that are formed due to the bridge breakup are longer and thicker than those formed from direct stretching of the corrugations.

At low Re_l and low We_g, the *LoLiD* process prevails. This is shown in Fig. 7 for a case at a very low $Re_l = 320$ and $We_g = 23\,000$ ($Oh_m = 0.475$). This case falls into Atomization Domain I as predicted in Fig. 3, i.e., lobes stretch directly into ligaments, without any perforations on the lobes. The ligaments that are formed at low Re_l are much thicker and longer than those of the higher Re_l, and the broken droplets are also larger. The results at high Oh and low density ratio (Fig. 7) are consistent with the numerical results of Jarrahbashi *et al.*[21] (see Figs. 25 and 26 of Ref. 21), the experimental results of Marmottant and Villermaux[14] for round liquid jets, and the numerical results of Scardovelli and Zaleski[16] (see Fig. 18 of Ref. 16) for planar liquid sheets.

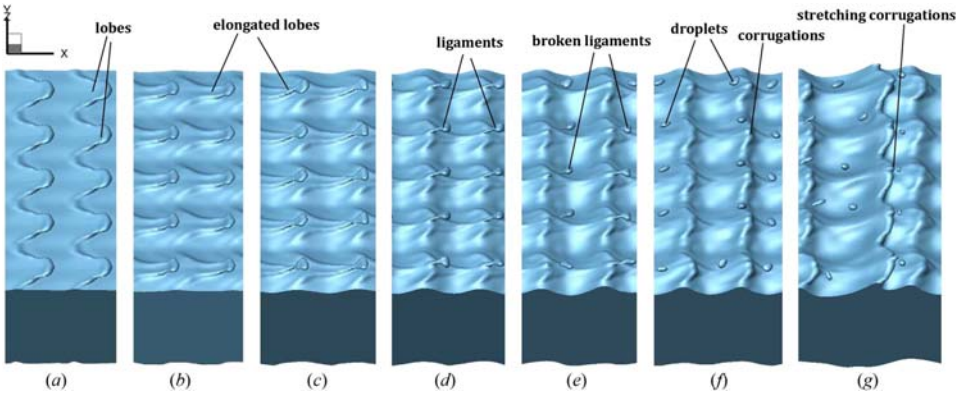

FIG. 7. Liquid surface showing the *LoLiD* process at low Re_l (Atomization Domain I), for a thick liquid sheet ($\Lambda = 0.5$) at low density ratio; $Re_l = 320$, $We_g = 23\,000$ ($Oh_m = 0.475$), $\hat{\rho} = 0.1$, and $\hat{\mu} = 0.0022$ at (a) 26 μs, (b) 36 μs, (c) 40 μs, (d) 44 μs, (e) 46 μs, (f) 48 μs, and (g) 52 μs.

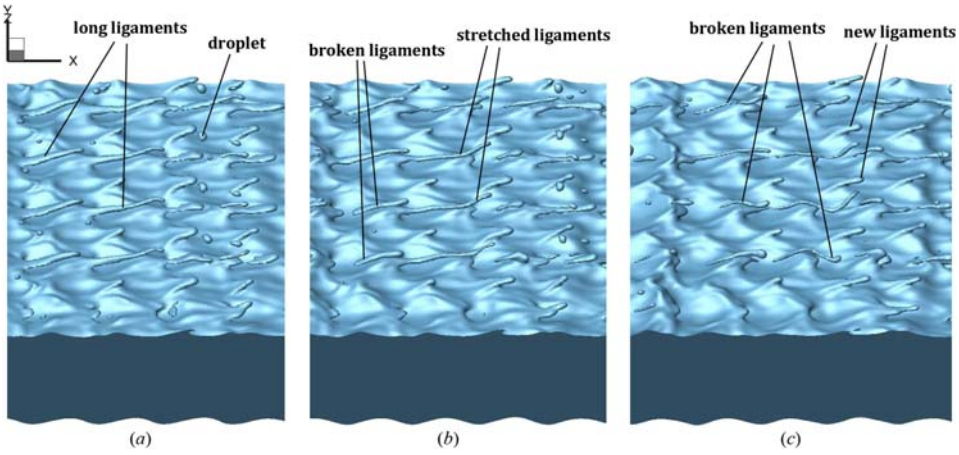

FIG. 8. Liquid surface deformation in Domain I through time, for a thick liquid sheet ($\Lambda = 0.5$) at low density ratio; $Re_l = 1000$, $We_g = 7200$ ($Oh_m = 0.085$), $\hat{\rho} = 0.1$, and $\hat{\mu} = 0.0022$ at (a) 40 μs, (b) 42 μs, and (c) 44 μs.

To clarify the breakup regimes at low Re_l and to understand the Re_l effects on the surface deformation better, lower Oh_m cases are studied by increasing Re_l and decreasing We_g. Figure 8 depicts the liquid surface deformation at $\hat{\rho} = 0.1$, $Re_l = 1000$, and $We_g = 7200$ ($Oh_m = 0.085$). This case still falls in Domain I. Since surface tension has increased and liquid viscosity is lower compared to that of Fig. 7, the ligaments are stretched longer; compare Figs. 7 and 8. The ligaments break at 42 μs and new ligaments are formed at the breakup location, as shown in Fig. 8(c) at $t = 44$ μs. The broken ligaments later break into droplets due to capillary instability; see Fig. 9. Corrugations are formed at the location of primary ligament breakup, which will stretch into new ligaments at a later time. The droplets and ligaments formed here are smaller and thinner than those of the lower Re_l shown in Fig. 7.

In Secs. III C–III E, the effects of density ratio, sheet thickness, and viscosity ratio are studied to give a more complete picture of the atomization categories. Afterwards, the contribution of different factors in formation of the streamwise vorticity is examined at high and low density ratios to establish the physical explanation required to better understand the role of density ratio in the cascade process. The characteristic time for each of these mechanisms is also determined in Sec. III H. The characteristic time scales guide us in normalizing (generalizing) the temporal behaviors, i.e., the cascade of the length scales and the sheet expansion.

C. Density-ratio effects

Since liquid Weber number (We_l) is usually used in the liquid jet atomization literature rather than We_g, it would be interesting to see the effects of density ratio on the atomization cascades using the We_l parameter. Gas-to-liquid density ratio ($\hat{\rho}$) has a clear effect on We_g; decreasing $\hat{\rho}$ at the same We_l decreases We_g. Figure 10 shows that increasing $\hat{\rho}$ brings the transitional boundary closer to the Re_l axis on a We_l–Re_l diagram. The lowest borderline in Fig. 10 is actually the same for the We_g–Re_l diagram also, since it represents a density ratio of unity ($We_l = We_g$ for $\hat{\rho} = 1.0$). As $\hat{\rho}$ is lowered, the transitional curve between Domains I/III and II moves to higher values in the We_l–Re_l diagram. This means that, in reality, the points with medium We_l, that were formerly in Domain II at higher $\hat{\rho}$, might fall in Domain I or III at the lower density ratio, i.e., a case that is closely above the borderline curve (in Domain II) for $\hat{\rho} = 1.0$ will fall below the borderline curve (in Domain I or III) if $\hat{\rho}$ is reduced to 0.1 at the same We_l. This is true for all data points in the area between the $\hat{\rho} = 0.1$ and $\hat{\rho} = 1.0$ curves. In conclusion, Domains I and III expand on the We_l–Re_l diagram as density ratio is lowered, and the lobe/ligament stretching becomes more dominant over a larger area of the We_l–Re_l diagram.

A case at low $\hat{\rho} = 0.1$ and low $Re_l = 320$ and high $We_l = 230\,000$ (in Domain I) was shown earlier in Fig. 7, which followed a *LoLiD* process in its early breakup. The same case but with a higher $\hat{\rho} = 0.5$ is shown in Fig. 11. Both cases are

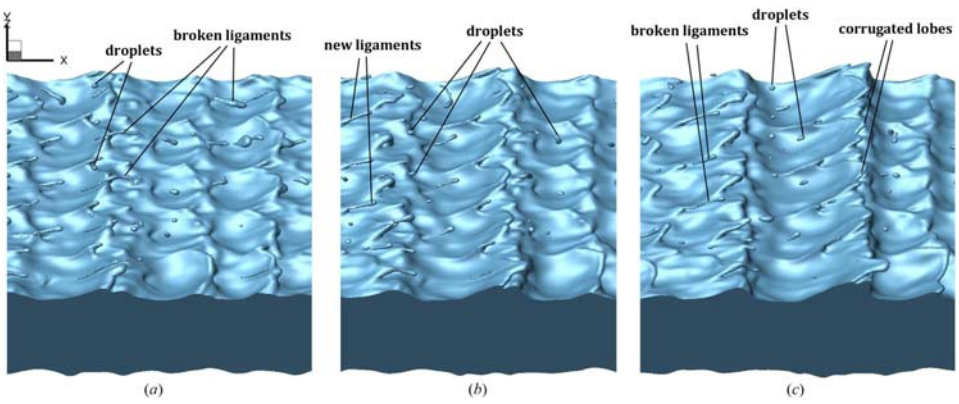

FIG. 9. Liquid surface deformation in Domain I at later times, for a thick liquid sheet ($\Lambda = 0.5$) at low density ratio; $Re_l = 1000$, $We_g = 7200$ ($Oh_m = 0.085$), $\hat{\rho} = 0.1$, and $\hat{\mu} = 0.0022$ at (a) 46 μs, (b) 48 μs, and (c) 50 μs.

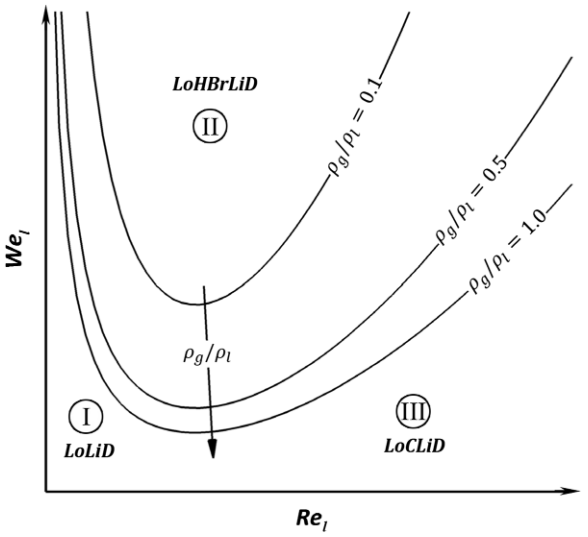

FIG. 10. Effect of density ratio on the atomization domains on a We_l–Re_l diagram.

at a very low Re_l but at a very high We_l, resulting in $Oh = 1.5$. However, We_g and Oh_m are different in these two cases due to the difference in $\hat{\rho}$. We_g of the case with $\hat{\rho} = 0.1$ was 23 000, which places this case under the transitional boundary curve in Figs. 3 and 10, i.e., in Domain I. However, as $\hat{\rho}$ is increased to 0.5, We_g becomes much higher (=115 000). Thus, the case with $\hat{\rho} = 0.5$ falls in Domain II on top of the transitional curve in both Figs. 3 and 10. Figure 11 shows the surface deformation for this case and manifests that its atomization cascade follows well our scenario, i.e., holes and bridges form and break into ligaments and droplets. This proves that density ratio has a substantial effect on the breakup process through We_g.

A closer look at Figs. 7 and 11 reveals that density ratio also affects the time scale of the droplet formation and the shape of the lobes. Droplets form much sooner and the lobes are more stretched at higher $\hat{\rho}$, which involves hole formation. The lobes are thinned in the spanwise (y) direction at lower $\hat{\rho}$ but in the normal (z) direction at higher $\hat{\rho}$.

D. Sheet thickness effects

Two different sheet thicknesses have been analyzed in this study: the thin sheet with $h = 50$ μm resulting in $\Lambda = 2.0$ and the thick sheet with $h = 200$ μm resulting in $\Lambda = 0.5$. The sheet thickness affects Oh_m ($=\sqrt{\hat{\rho}}\mu_l/\sqrt{\rho_l h\sigma}$); therefore, it can change the atomization characteristics especially at high Re_l, even at constant fluid properties and flow velocity. Recall that the transitional boundary between Domains II and III is a parabolic curve with constant Oh_m (see Fig. 3). A thicker jet would have smaller Oh_m at the same flow conditions and the same fluid properties; thus, with increasing sheet thickness, the atomization cascade would move away from Domain II, toward Domain III, as Oh_m is lowered below the critical $Oh_m \approx 0.021$ (see Fig. 3).

The sheet thickness effects are embedded in We_g and Re_l parameters, and it does not change the atomization characteristics on its own if We_g and Re_l are kept constant. The case shown in Fig. 12 has the same Re_l, We_g, and $\hat{\rho}$ as those of Fig. 11, but with a thinner sheet ($h = 50$ μm compared to 200 μm in Fig. 11). The results show that the sheet thickness alone does not alter the atomization mechanism, as both thin and thick sheets (Figs. 12 and 11, respectively) manifest the same *LoH Br LiD* cascade process. An increase in the sheet thickness delays the breakup process, thus affecting the time scales of the structure cascade and droplet formation. This will be discussed in Sec. III H.

E. Viscosity ratio effects

In order to check the effects of viscosity ratio ($\hat{\mu}$) on the atomization cascades and their time scales, different viscosity ratios in the range $O(10^{-3}) < \hat{\mu} < O(10^{-1})$ have been studied at several different Re_l's and We_g's in each domain. Figure 13(a) compares the surface of two liquid sheets with different viscosity ratios at 22 μs—both in Atomization Domain II. Even though the viscosity ratios are two orders of magnitude apart, the surfaces are very similar. Both cases follow the *LoH Br LiD* cascade process, and the size and shape of the holes and bridges (ligaments) are very similar at each time; the lower $\hat{\mu}$ case manifests slightly larger perforations. Figure 13(b) also compares two very different $\hat{\mu}$ cases from Atomization Domain III. Both cases follow the *LoC LiD* process, and the size and shape of lobe corrugations and ligaments are fairly equal at 50 μs.

From the above discussion and the results illustrated in Fig. 13, it is concluded that $\hat{\mu}$ does not alter the atomization process; thus, the threshold between Domains I/III and II (the

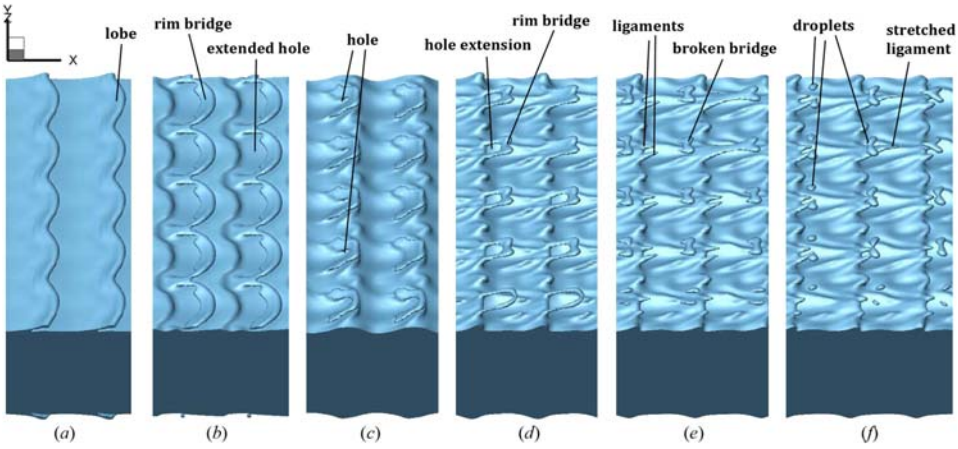

FIG. 11. Liquid surface deformation in Domain II through time, for a thick liquid sheet ($\Lambda = 0.5$) at high $\hat{\rho}$; $Re_l = 320$, $We_g = 115\,000$ ($Oh_m = 1.05$), $\hat{\rho} = 0.5$, and $\hat{\mu} = 0.0022$ at (a) 18 μs, (b) 22 μs, (c) 26 μs, (d) 28 μs, (e) 30 μs, and (f) 32 μs.

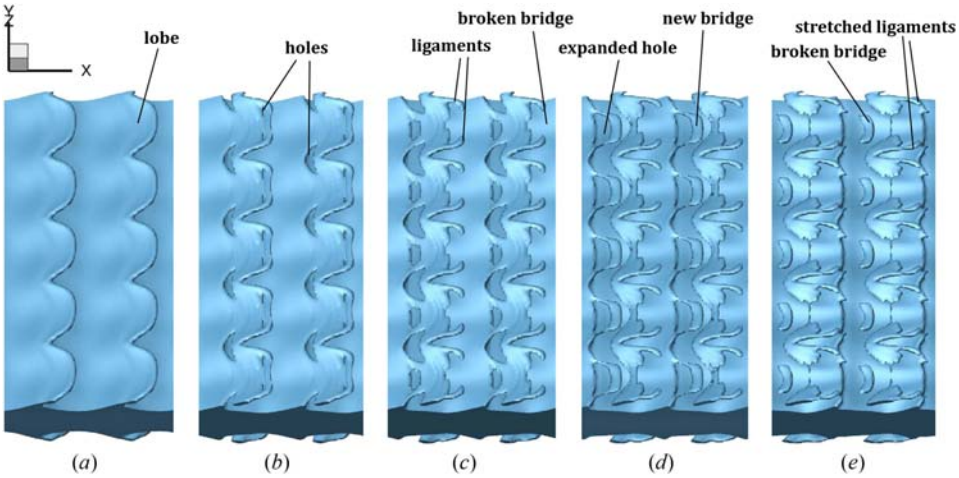

FIG. 12. Liquid surface deformation in Domain II through time, for a thin liquid sheet ($\Lambda = 2.0$); $Re_l = 320$, $We_g = 115\,000$ ($Oh_m = 1.05$), $\hat{\rho} = 0.5$, and $\hat{\mu} = 0.0022$ at (a) 10 μs, (b) 11 μs, (c) 12 μs, (d) 13 μs, and (e) 14 μs.

transitional region) is independent of $\hat{\mu}$, which also has a negligible effect on hole formation and lobe/ligament stretching time scales. In other words, the ligament stretching mechanism is liquid dominated, as far as the viscosity is concerned, i.e., the gas viscosity does not have a substantial role in ligament stretching. However, the gas density is significant in the hole formation mechanism as discussed before.

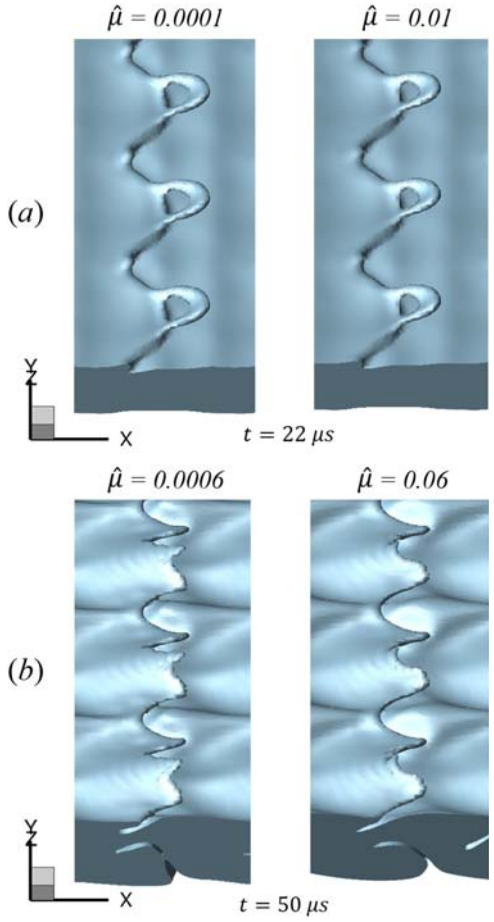

FIG. 13. Liquid surface deformation for two different viscosity ratios in Domain II; $Re_l = 2500$, $We_g = 7250$, $\hat{\rho} = 0.5$ (a); liquid surface deformation for two different viscosity ratios in Domain III; $Re_l = 5000$, $We_g = 7250$, $\hat{\rho} = 0.5$ (b). The time of each frame and the viscosity ratios are denoted on the images.

F. Streamwise vorticity generation

The streamwise vorticity (ω_x) is crucial to understand the origin of the three-dimensional instability on liquid jets. The effects of density ratio on the streamwise vorticity generation are studied in detail by Zandian *et al.*[29] The most pertinent findings of Ref. 29 are repeated in this section to help us understand the differences that are observed on the liquid surface structure due to the vortical structures at high and low density ratios. The goal here is to explain the different atomization cascades that are seen at low ($\hat{\rho} = 0.05$) and high density ratios ($\hat{\rho} = 0.5$) from a vorticity dynamics perspective.

The complete form of the vorticity equation is

$$\frac{D\boldsymbol{\omega}}{Dt} = (\boldsymbol{\omega}\cdot\nabla)\mathbf{u} - \boldsymbol{\omega}(\nabla\cdot\mathbf{u}) + \nabla\times\left(\frac{\nabla\cdot\tau}{\rho}\right) + \frac{1}{\rho^2}\nabla\rho\times\nabla p + \nabla\times \mathrm{F}_\sigma, \tag{15}$$

where $\mathbf{u}$ and $\boldsymbol{\omega}$ are the velocity and vorticity vectors, respectively. τ is the viscous stress tensor, and F_σ is the surface tension force. Since the fluids are incompressible in this study, the second term on the right-hand side is zero. The surface tension (last term) and the viscous diffusion terms (third term on the right-hand side) have negligible contribution to the vorticity generation; thus, the rate of change of ω_x is approximately

$$\frac{D\omega_x}{Dt} = \omega_x\frac{\partial u}{\partial x} + \omega_y\frac{\partial u}{\partial y} + \omega_z\frac{\partial u}{\partial z} + \frac{1}{\rho^2}\left[\frac{\partial\rho}{\partial y}\frac{\partial p}{\partial z} - \frac{\partial\rho}{\partial z}\frac{\partial p}{\partial y}\right], \tag{16}$$

where $\omega_x, \omega_y, \omega_z, u, \rho$, and p denote the streamwise, spanwise, and cross-stream (normal) vorticities, streamwise velocity, density, and pressure, respectively. The terms on the right-hand side denote streamwise stretching, spanwise tilting, normal tilting, baroclinic effect due to normal pressure gradient, and baroclinic effect due to spanwise pressure gradient, respectively. The component of pressure gradient that is tangential to the liquid-gas interface accounts for the tangential body force acting on the liquid at that interface. Density gradient is normal to the liquid interface, i.e., initially approximate in the z direction. The density gradient in y, i.e., $\partial\rho/\partial y$, is negligible compared to $\partial\rho/\partial z$, since the sheet cross section remains fairly rectangular for early instability development. Yet, this

term accounts for the baroclinic effect, which can deform the interface in the spanwise direction.

Except for numerical errors which, for our purpose, correspond to small random physical disturbances, all terms in the ω_x generation equation [Eq. (16)] are initially zero. Namely, the first and the third terms are zero because there are no vorticity components in the x- and z-directions initially, and the second term is zero since the streamwise velocity is uniform in the spanwise direction. The baroclinic terms are identically zero since density and pressure gradients in the y-direction are initially zero.

The terms in Eq. (16) are named as follows:

- Streamwise vortex stretching: $\omega_x \frac{\partial u}{\partial x}$.
- Spanwise vortex tilting: $\omega_y \frac{\partial u}{\partial y}$.
- Normal vortex tilting: $\omega_z \frac{\partial u}{\partial z}$.
- Baroclinic vorticity generation: $\frac{1}{\rho^2}\left[\frac{\partial \rho}{\partial y}\frac{\partial p}{\partial z} - \frac{\partial \rho}{\partial z}\frac{\partial p}{\partial y}\right]$.

Two cases have been analyzed in this section, which differ only in density ratio. The nondimensional characteristics of these two cases are as follows: $Re_l = 2500$, $We_l = 14\,400$, $\hat{\mu} = 0.0066$, and $\hat{\rho} = 0.05$ and 0.5. The sheet thickness is $h = 50$ μm, and no initial perturbation is imposed on the liquid-gas interface.

Zandian *et al.*[29] show that baroclinicity is the most important factor in ω_x generation at low density ratio; however, at high density ratio, baroclinicity is the least significant factor. The baroclinic vorticity generation term is an order of magnitude smaller than the vortex stretching and tilting terms overall.

Figure 14 shows the contours of the four ω_x generating terms for low density ratio at 13 μs on a y-plane. The spanwise and normal vortex tilting terms [Figs. 14(b) and 14(c)] are stronger than the streamwise stretching but with opposite signs. Zandian *et al.*[29] showed that the spanwise and normal vortex tilting terms, even though the largest among the ω_x generating terms, are not the most important in ω_x generation, since they nearly cancel each other. Therefore, the streamwise vortex stretching and baroclinic effects are the most important in generation of ω_x, at high and low density ratios, respectively.

Figure 14(a) also confirms that the vortex stretching originates on the braids first, as the strain due to the adjacent primary vortical structures is highest at the saddle (braid) and the ribs are aligned along the diverging separatrix.[30] Most of the colored spots in Fig. 14(a) are on the braids and not the wave crests. This is consistent with the experimental observations of earlier researchers[31–33] for uniform-density flows. The saddle points are in the gas phase, close to the interface. The streamwise vortex stretching is highest at the saddle points [see Fig. 14(a)], where the flow is primarily discrete ribs.[30] The fluid elements are stretched along the interface and compressed normal to the interface at the saddle points.

The stretching and tilting terms are centered at the interface [Figs. 14(a)–14(c)], but the baroclinic torque term $\frac{1}{\rho^2}\nabla\rho\times\nabla p$ is always larger in the gas phase [Fig. 14(d)].

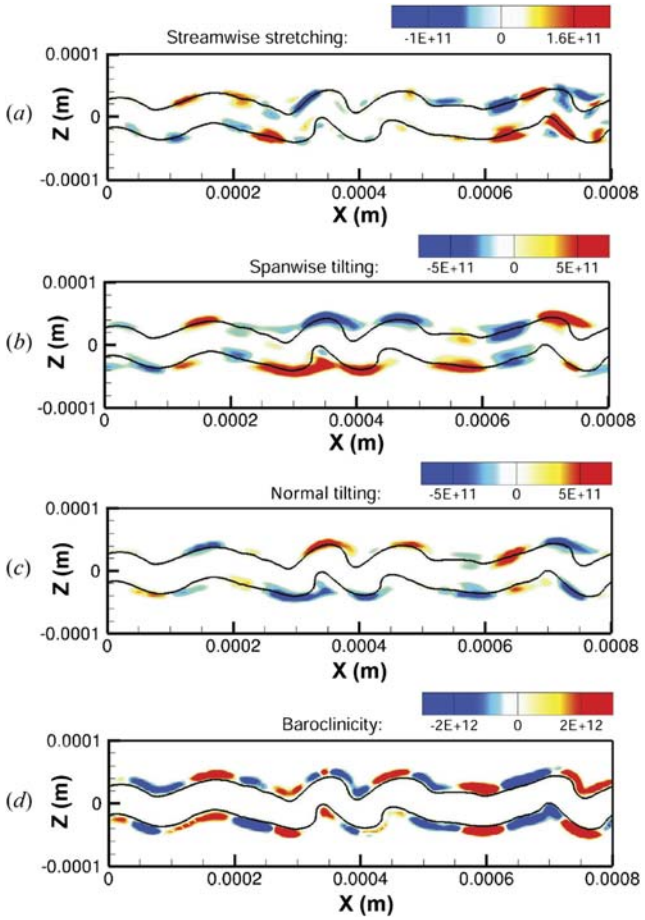

FIG. 14. Contours of the streamwise vortex stretching (a), spanwise vortex tilting (b), normal vortex tilting (c), and baroclinic generation (d) on a y-plane at $t = 13$ μs for $\hat{\rho} = 0.05$; $Re_l = 2500$, $We_l = 14\,400$, and $\hat{\mu} = 0.0066$.

Baroclinic generation, being proportional to $1/\rho^2$, is two orders of magnitude larger in the gas phase compared to the liquid phase (for $\hat{\rho} = 0.05$). As $\hat{\rho}$ increases, the difference between the gas and liquid densities decreases; thus, the contours of baroclinicity get closer to the liquid interface. This is seen in the baroclinicity contours of $\hat{\rho} = 0.5$ in Fig. 15. Since density ratio is an order of magnitude higher than that of Fig. 14(d), the local density in the gas zone is much higher; hence, the baroclinicity in the gas is lower and closer to its value in the liquid. Therefore, the contours are closer to the interface [compare Figs. 15 and 14(d)]. This contributes to the ω_x peak being closer to the interface and growing larger compared to the low density ratios, thereby creating and stretching more lobes at higher density ratios. Also, the peak of baroclinic

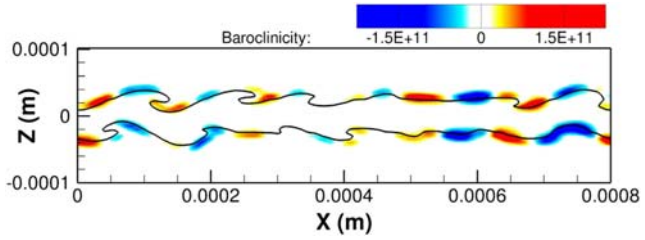

FIG. 15. Contours of baroclinicity on a y-plane at $t = 13$ μs for $\hat{\rho} = 0.5$; $Re_l = 2500$, $We_l = 14\,400$, $\hat{\mu} = 0.0066$.

torque is an order of magnitude smaller in Fig. 15 compared to Fig. 14(d), since the density gradient normal to the interface is lower at higher density ratios.

As shown in Fig. 14(d), the baroclinicity contours change sign (i.e., color) continuously in x. This pattern is very similar to the hairpin pattern seen in the ω_x contours presented by Jarrahbashi and Sirignano.[20] The ω_x and ω_y contours for the current case are illustrated in Fig. 16. Comparison of the contours of ω_x and baroclinicity [Figs. 16(a) and 14(d)] shows that they follow a very similar pattern. Therefore, we can conclude that baroclinicity is the most important factor in creation of the hairpin vortex structure at low density ratios. The role of the baroclinic torque in deformation of the surface waves in a stratified shear layer is studied in detail by Schowalter *et al.*[34] and is consistent with our results. The vorticity contours of Fig. 16 show that ω_x and ω_y are largest at the braids and the wave crests, respectively. Interestingly, the ω_y peak coincides with the interface at the crests but not at the troughs [Fig. 16(b)], where the vorticity has migrated (diffused) into the gas phase, further away from the interface.

The magnitude of the vorticity components was also examined for the high and low density ratios through time by Zandian *et al.*[29] The 3D instabilities are directly related to the magnitude of ω_x and ω_z against ω_y, which exists from the beginning when the flow is still 2D. As mentioned earlier by Jarrahbashi *et al.*[20,21] and Zandian *et al.*,[22] streamwise vorticity is the main cause of three-dimensional instabilities. Zandian *et al.*[29] showed that ω_y is larger at lower density ratios. ω_x and ω_z grow very slowly in the beginning, but their growth rate suddenly increases after the initial period. The growth rate of ω_x is higher at higher density ratios. Therefore, three-dimensionality manifests sooner at higher gas densities. The growth rate of ω_x is lower at lower $\hat{\rho}$. Thus, ω_y is still dominant at low gas densities and 2D deformations build up while the streamwise vorticity grows. ω_x growth has consequent impacts on the surface dynamics. In order to understand this, the liquid surface has been compared at two instances for both low and high density ratios in Fig. 17. The boxes in this figure show the computational domain edges. The boundary remains far away from the liquid surface; hence the results are not influenced by the domain size.

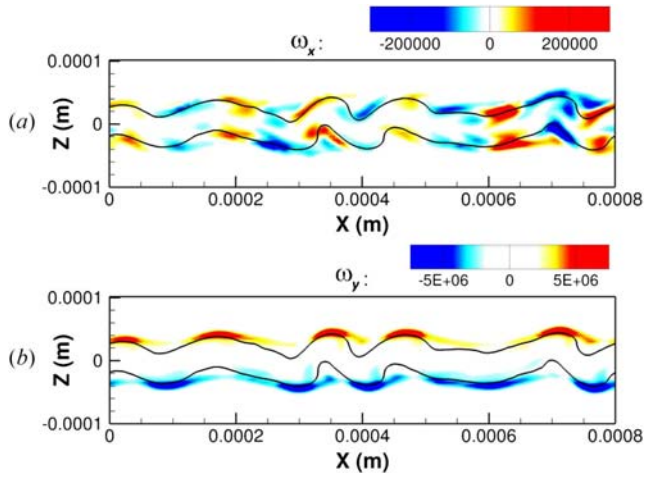

FIG. 16. Contours of the streamwise vorticity (a), and the spanwise vorticity (b) at t = 13 μs for $\hat{\rho}$ = 0.05; Re_l = 2500, We_l = 14 400, $\hat{\mu}$ = 0.0066.

The higher ω_x growth rate at high density ratio causes the liquid surface to undergo 3D instabilities faster, and there are more streamwise lobes seen at high $\hat{\rho}$ than at low $\hat{\rho}$. At 15 μs, the surface of the sheet with $\hat{\rho}$ = 0.05 is still roughly two-dimensional, while the high density-ratio case manifests more 3D deformations, and streamwise lobes are apparent on top of the primary KH waves. On the other hand, the higher ω_y compared to ω_x at low $\hat{\rho}$ causes the liquid sheet to become asymmetric much faster (compare the top images of Fig. 17).

The difference in the vorticity dynamics in the two cases has significant effects on the characteristics of the jet instabilities. As can be seen in Fig. 17 at t = 18 μs, the low $\hat{\rho}$ case can be characterized by roll-up of the KH waves, which creates more spanwise-aligned liquid structures and fewer stretched lobes; the entire sheet thins faster, and the liquid sheet breaks sooner. On the other hand, at high $\hat{\rho}$, the liquid structures orient streamwise more and manifest more lobes. The lobes are more stretched and thinned due to the larger ω_x and are more prone to perforation. Thus, the hole-formation mechanism is expected to prevail over a larger area in the parameter space of We_l versus Re_l, at higher density ratios. This is consistent with the domains in Figs. 3 and 10 and is in accordance with the density-ratio effects discussed in Sec. III C.

The top and bottom liquid surfaces tend toward an antisymmetric mode, whether we start with a flat surface or symmetric perturbations. The antisymmetric behavior is eventually favored as a plane jet is more unstable to the antisymmetric than the symmetric mode in the parameter range of practical interest.[5] The transformation toward antisymmetry occurs sooner as density ratio is lowered.

G. Comparison with other planar and round jet computations

In order to verify our findings of the atomization categories in the We_g–Re_l map and to check their dependence on the jet geometry (planar vs. circular), a similar diagram for round liquid jets has been built using the numerical results of Jarrahbashi *et al.*[21] In their work, both *Re* and *We* are based on the initial liquid jet diameter. Their values are transformed to We_g and Re_l based on jet radius for the purpose of comparison. The results of other numerical studies (Refs. 17–19) are also compared qualitatively, where possible.

All of the cases studied by Jarrahbashi *et al.*[21] are shown in the We_g–Re_l plot in Fig. 18 (right plot). The cases are grouped into the three atomization categories we introduced, i.e., *LoH Br LiD*, *LoLiD/LoC LiD* (stretching either with or without corrugations), and the transitional domain. Since frame by frame surface deformation at the early breakup stages was not given in Ref. 21, clear distinction between the two stretching mechanisms was not possible, hence both *LoLiD* and *LoC LiD* cases were put in the same group (denoted by squares in Fig. 18). Even though most of their results were for low Re_l and high We_g, they show some similarity in behavior with the planar liquid jets in different domains. With the newly defined Re_l and We_g based on the jet radius, instead of

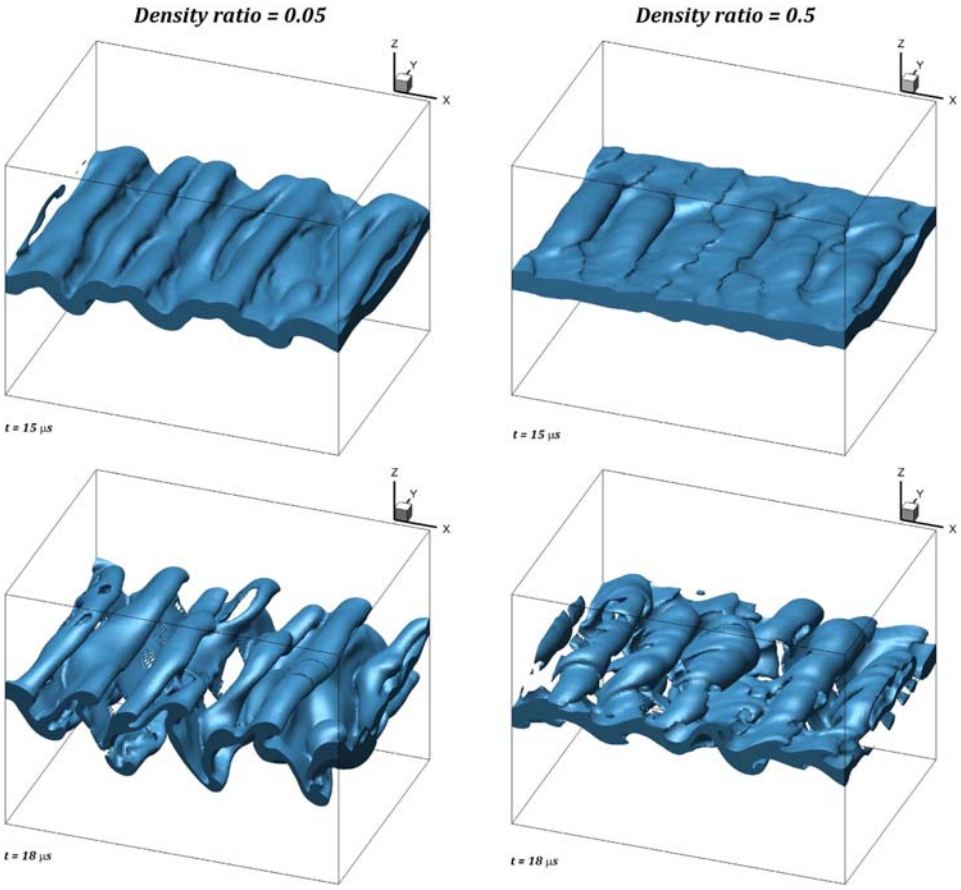

FIG. 17. The liquid-gas interface at $t = 15\,\mu$s (top) and $t = 18\,\mu$s (bottom) for $Re_l = 2500$, $We_l = 14\,400$, $\hat{\mu} = 0.0066$; $\hat{\rho} = 0.05$ (left), $\hat{\rho} = 0.5$ (right).

the diameter, all of the data points fall in the proper zones in this diagram without notably altering the domain's boundary. The transitional boundary follows the same Eq. (13), with the coefficients

$$a = 0.816, \quad b = 1.07, \quad c = -0.4, \quad \epsilon = 0.04, \qquad (17)$$

and the same reference values for Re_l and We_g, i.e., $Re_r = 2500$ and $We_r = 4900$. Only b has changed from the planar jet result. Above this transitional boundary, the hole formation mechanism prevails and below this curve the lobe/ligament stretching is the primary atomization cascade.

The left plot in Fig. 18 shows the hyperbolas that bound the atomization regime from the three other regimes of a round liquid-jet breakup presented by Reitz and Bracco[7] (following the original work of Ohnesorge[8]), on a blown-up view of the lower left corner of our diagram on the right. The purpose of putting these two plots side-by-side in Fig. 18 is to emphasize that the Atomization Domain dwarfs the other domains in both parameter range and importance in practical spray formation. Yet, surprisingly this domain is the least studied of all.

Re_l for the planar liquid sheets studied by Desjardins and Pitsch[17] was in the range 2000–3000, and the highest We_g in their study was $O(10^2)$, which as they assert, puts all their cases in the second wind-induced breakup regime (see the left image in Fig. 18), even though this regime was originally described

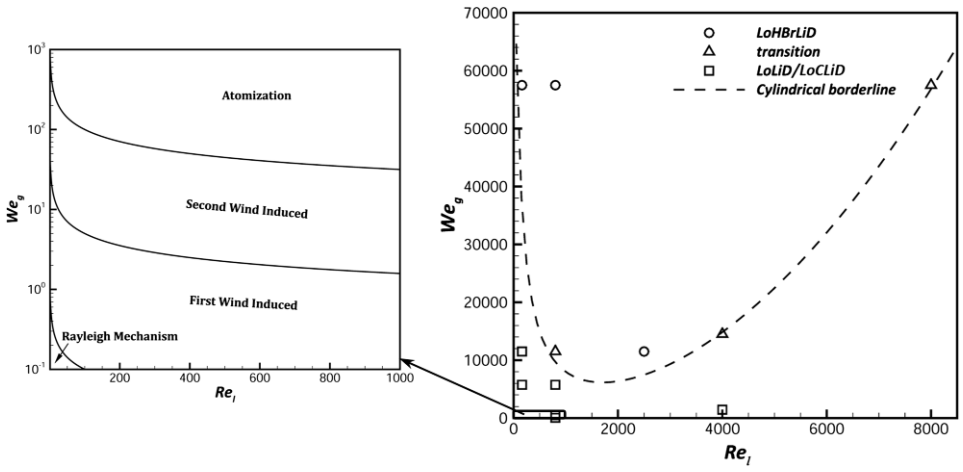

FIG. 18. The operation regimes of a round liquid-jet breakup by Reitz and Bracco[7] recast on a We_g (log-based) vs. Re_l plot (left). The breakup characteristics based on Re_l and We_g (using jet radius) for round liquid jets, from the results of Jarrahbashi *et al.*[21] (right). The three breakup categories are shown by symbols, along with the transitional boundary obtained from planar liquid sheet diagram with minor modification (dashed line).

for round jets.[7] Thus, all their results could be considered to be in the *LoLiD* group in our classification. Even though only a few figures at different steps of sheet breakup were presented there, they summarized the atomization processes in three essential steps: (i) initial corrugation of the interface (i.e., formation of lobes); (ii) formation and stretching of liquid ligaments; and (iii) rupture of the ligaments, leading to droplet formation. They also mention that the ligaments are typically oriented in the streamwise direction, and there is no sign of hole formation in their results.

Shinjo and Umemura[18] studied a smaller range of Re_l (<1500) and slightly higher We_g (<500) than Desjardins and Pitsch[17] for a round liquid jet. They studied startup of a full liquid-jet injected into a gas, including the shredding of the cap. The range of Re_l and We_g puts their cases in the *LoLiD* group. The strong shear near the liquid surface deforms the liquid surface, inducing ligament formation, as described by Shinjo and Umemura.[18] They suggest that the main mechanism for ligament formation is the stretching of the sheared liquid surfaces (lobes); however, most of the ligaments and droplets are formed near the mushroom-shaped tip of the jet and not the main body of the liquid jet, and ligament formation occurs first from the tip edge. They also observed hole formation on the lobes; however, it was not due to the vortex motion but due to the inertial motion from the re-collision of the broken droplets from the tip edge. Hence, the hole-formation mechanism seen in their study is different from ours, since the jet tip physics are not included in our study of the liquid-sheet segment. Herrmann[19] studied a round liquid jet with similar range of We_g as Shinjo and Umemura and slightly higher Re_l (=2500) (based on nozzle radius). He did not witness any hole formation in the liquid jet breakup, and only ligament stretching was observed. Since his Re_l was higher than that of Shinjo and Umemura, more corrugations and smaller and thinner ligaments were observed in his study, which is in agreement with our findings.

The experimental results of Hoyt and Taylor[13] for round liquid jets at a very high Reynolds number of $O(10^5)$ show similar atomization characteristics with very small corrugations and very thin ligaments as our results for Domain III. Even though their study focuses on spatial development of a liquid jet and ours is temporal, a qualitative comparison with their results shows that as Re_l increases, the length scale of the ligaments and corrugations becomes smaller—consistent with what has been found here.

From the analysis in this section, we conclude that the atomization domains are generic, fairly independent of the liquid jet geometry. The same domains can be classified on the We_g–Re_l diagram with very minor modifications for both planar and round liquid jets.

H. Structure cascade time scales

As mentioned earlier, there are two different characteristic times for the formation of holes and the stretching of lobes and ligaments. At the same Re_l (high Re_l), as the surface tension increases (decreasing Oh and We_l), the characteristic time for hole formation becomes larger, delaying the hole formation. Thus, for lower Oh (or We_l), most of the earlier ligaments are formed due to direct stretching of the lobes and/or corrugations, while the hole formation is halted. On the other hand, at relatively large Re_l (>3000), as liquid viscosity is increased (decreasing Re_l and increasing Oh), at the same We_l, the ligament-stretching time gets larger. In this case, hole formation prevails compared to the ligament stretching mechanism, resulting in more holes on the liquid lobes.

Figure 19 shows the first time at which a hole forms for three different We_l's at high $Re_l = 5000$ and high $\hat{\rho} = 0.5$. The other dimensionless parameters are the same for all three cases. As We_l increases, from left to right, the hole formation time decreases. The first hole is formed at 52 μs for $We_l = 14\,400$ (the left image) and at around 13 μs for $We_l = 72\,000$ (the right image). This indicates that the hole formation characteristic time should be inversely proportional to We_l. The holes expand more rapidly at higher We_l. At high Re_l, the hole formation is delayed as $\hat{\rho}$ decreases. Thus, the hole-formation time scale should also be inversely proportional to $\hat{\rho}$. This effect may be combined with the effect of We_l by using the gas We_g rather than the liquid We_l.

The time scales are nondimensionalized using the freestream gas velocity (U) and the sheet thickness (h) as characteristic velocity and length. Figure 20 shows the nondimensional lobe/ligament stretching time scale ($U\tau_s/h$) as a function of Re_l at several We_g's. τ_s is the dimensional characteristic time for ligament stretching and corresponds to the first

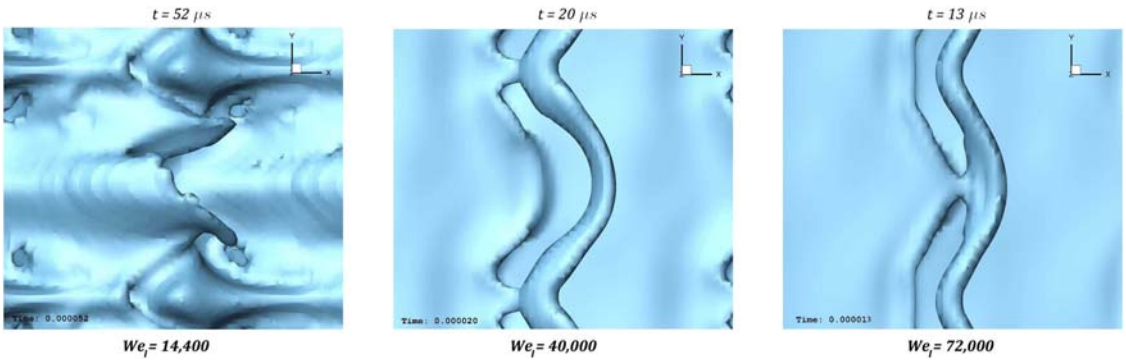

FIG. 19. The time at which the first hole forms at different We_l's; $Re_l = 5000$, $\hat{\rho} = 0.5$, and $\hat{\mu} = 0.0066$. The time and We_l are indicated at top and bottom of each image, respectively.

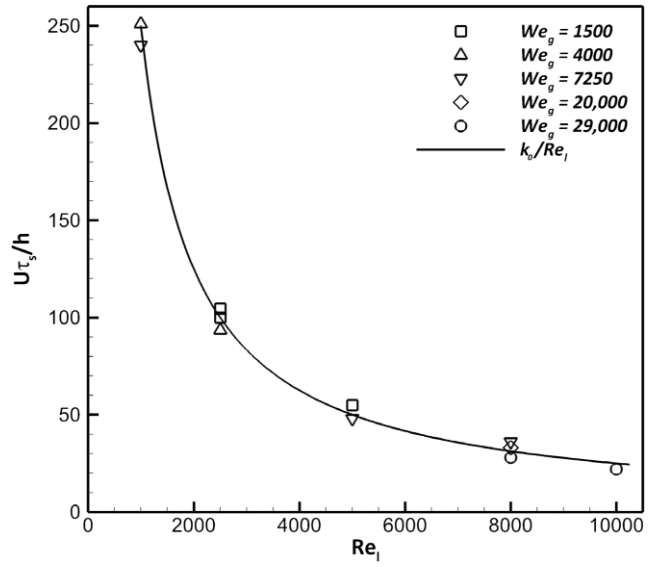

FIG. 20. Nondimensional stretching time scale versus Re_l at different We_g's.

time when a ligament is formed. The stretching time scale is proportional to the reciprocal of Re_l and has negligible dependence on We_g (see Fig. 20). All of the cases at We_g values from 1500 to 29 000 fit well on the same curve k_0/Re_l; k_0 is a nondimensional constant.

Based on the results presented in Figs. 19 and 20, two different characteristic times are formed at high Re_l—one for each mechanism—involving surface tension and viscosity. The hole-formation characteristic time (τ_h) is directly proportional to the surface tension and inversely proportional to the density ratio, while the stretching characteristic time (τ_s) is proportional to the liquid viscosity. Thus, the following two nondimensional characteristic times are proposed for these mechanisms:

$$\frac{U\tau_s}{h} \propto \frac{\mu_l}{\rho_l U h} = \frac{1}{Re_l}, \tag{18}$$

$$\frac{U\tau_h}{h} \propto \frac{\sigma}{\rho_g U^2 h} = \frac{1}{We_g}. \tag{19}$$

As indicated in the equations above, the characteristic times can be written in terms of the sheet thickness and jet velocity. In this form, the hole-formation nondimensional time becomes inversely proportional to We_g, while the stretching nondimensional time is inversely related to Re_l. However, real times are independent of the thickness and only depend on the fluid properties. Clearly, h/U is a convenient normalizing time. Aside from its accord with our results, these time scales are consistent with intuition. The surface tension hinders hole formation, thus increasing its time scale, while liquid viscosity resists stretching, hence increasing the stretching characteristic time. Also, the time scales for both mechanisms become larger for the same dimensionless parameters as the jet becomes thicker. The case with $Re_l = 2500$ and $We_g = 7250$ and $h = 200$ μm perforates first at around 82 μs (Fig. 4), while a jet with the same Re_l and We_g, and $h = 50$ μm perforates at around 20 μs, which is almost 4 times less than that of the thicker sheet.

Combination of Eqs. (18) and (19) yields a relation between the two time scales at high Re_l regions of interest, involving Oh_m,

$$\frac{U\tau_h}{h} \propto \left(\frac{U\tau_s/h}{Oh_m}\right)^2. \tag{20}$$

In the transitional region, near the boundary, where the two characteristic times are of the same order, both hole formation and corrugation stretching appear at different parts of the liquid surface, as shown in Fig. 6.

At low Re_l (<3000) range, the liquid viscosity has an opposite effect on the hole formation and ligament stretching. As shown in Fig. 3, near the left boundary, the time scale of the stretching becomes relatively smaller than the hole-formation time scale as Re_l is reduced at a constant We_g. Hence, there is a move back to ligament stretching from hole formation with decreasing Re_l at a fixed We_g. It is concluded that a term should

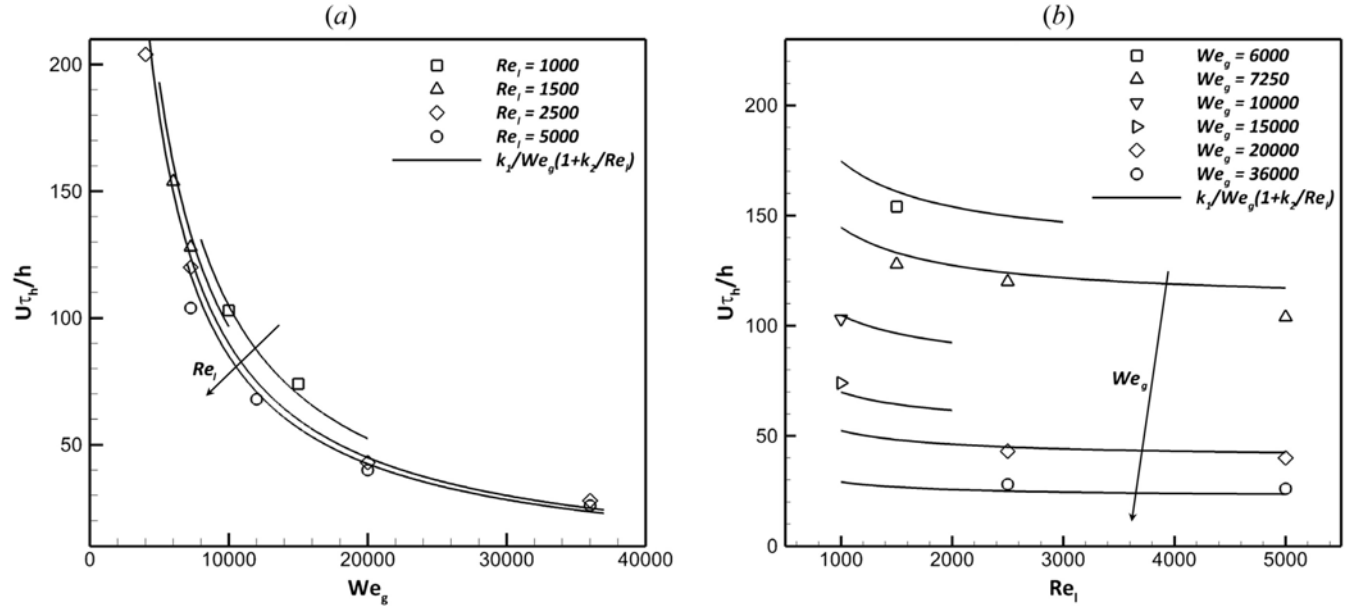

FIG. 21. Nondimensional hole-formation time scale versus We_g at different Re_l's (a) and versus Re_l at different We_g's (b).

be added in the hole-formation time scale, which becomes larger at lower Re_l. At higher Re_l, however, this term would vanish, with a return to the time scale in Eq. (19). In order to generalize the hole-formation time scale, a term is added with the reciprocal of Re_l as its coefficient to fix the opposite behavior seen at lower Re_l. The new, more general, nondimensional time scale then becomes

$$\frac{U\tau_h}{h} \propto \frac{\sigma}{\rho_g U^2 h}\left(1+\frac{k}{Re_l}\right) = \frac{1}{We_g}\left(1+\frac{k}{Re_l}\right), \qquad (21)$$

where k is a nondimensional constant. The stretching time scale does not need any modification for low Re_l (see Fig. 20).

Figure 21(a) shows the nondimensional hole-formation time scale versus We_g at different Re_l's. The hyperbolic relation between the hole-formation time scale and We_g at any constant Re_l is evident. As Re_l decreases, the hyperbolas shift upward. The solid lines represent Eq. (21), where k_1 and k_2 are nondimensional constants. As Re_l increases, the hyperbolic curves get closer to one another, meaning that the effect of Re_l becomes less important at higher Re_l. At very high Re_l, the term in parenthesis in Eq. (21) approaches unity and Eq. (19) is retained.

The results shown in Fig. 21(a) indicate that Re_l is not as unimportant as We_g was for τ_s (shown in Fig. 20). Figure 21(b) shows the dependence of the hole-formation time scale on Re_l at different We_g values. At a constant We_g, the nondimensional hole-formation time is a hyperbolic function of Re_l but with a much slighter slope in the range considered here. As We_g increases, these hyperbolas (solid lines) move down in Fig. 21(b). The dependence of τ_h on We_g compared to Re_l becomes clear as we compare Fig. 21(b) with Fig. 21(a). At very high We_g [the bottom curves in Fig. 21(b)], the hole-formation characteristic time becomes almost independent of Re_l for the range of Re_l considered in this plot. The solid lines become almost straight horizontal lines as We_g becomes very large.

Combining Eqs. (18) and (21), the relation between the two time scales becomes

$$\frac{U\tau_h}{h} \propto \left(\frac{U\tau_s/h}{Oh_m}\right)^2\left(1+\frac{k}{Re_l}\right). \qquad (22)$$

At high Re_l (>3000), the second parenthesis approaches unity and the earlier derived relation in Eq. (20) is retained. At very low Re_l limit (<200), the asymptotic relation between the two time scales becomes

$$\frac{U\tau_h}{h} \propto \frac{1}{Re_l}\left(\frac{U\tau_s/h}{Oh_m}\right)^2 = \frac{Re_l}{We_g}\left(\frac{U\tau_s}{h}\right)^2. \qquad (23)$$

So, at low Re_l, the hole formation and the ligament stretching time scales are not related only by the modified Ohnesorge number; the flow Re_l also has a substantial role in the atomization cascade at low Re_l.

IV. CONCLUSIONS

Temporal development of surface waves on planar jets and their breakup into droplets are studied numerically. Three main atomization cascades are identified. The atomization characteristics are well categorized on a parameter space of gas Weber number (We_g) versus liquid Reynolds number (Re_l). The gas-to-liquid density ratio affects the breakup process, thereby making We based on liquid density less important as a correlation factor. The Rayleigh domain, the first wind-induced domain, and the second wind-induced domain collectively occupy a minor portion of the We_g vs. Re_l diagram. Furthermore, the atomization portion is now separated as three subdomains. Atomization Domain I has a lobe-ligament-droplet (*LoLiD*) cascade; Domain II involves a lobe-hole-bridge-ligament-droplet (*LoH Br LiD*) cascade; and Domain III shows a lobe-corrugation-ligament-droplet (*LoC LiD*) cascade.

At high Re_l, the breakup characteristics change based on a modified Ohnersorge number ($Oh_m = \sqrt{We_g}/Re_l$). At high Oh_m, the lobes thin and perforate to form bridges, which eventually break into one or two ligaments. At lower Oh_m, the hole formation is hindered and instead, the lobe rims corrugate and stretch into small ligaments. There is also a transitional region, where both mechanisms co-exist. The transition region at high Re_l follows a constant Oh_m line.

At low Re_l, the transitional region follows a hyperbolic function in the We_g–Re_l plot. At low We_g and low Re_l, the lobes stretch directly into ligaments. The ligaments created in this domain are fairly thick and long, and result in larger droplets. As We_g is increased while keeping Re_l low, the hole formation process prevails. Thus, the hole formation process dominates over a wide range of low and high Re_l but only over moderate to high We_g. Below a critical We_g, hole formation is completely hindered at all Re_l. At lower density ratios, streamwise vorticity grows slower and its peak departs from the interface toward the gas zone. This enhances the gas entrainment, but the lobes do not stretch enough to thin and perforate. Thereby, ligament stretching is more dominant while hole formation only occurs at much higher We_g. These atomization cascades are independent of the jet geometry (planar or round). Furthermore, a very similar correlation describes the boundaries between different atomization domains for the planar and round jets.

Viscosity ratio has no substantial effect either on the cascade processes or their time scales, while the effect of sheet thickness is described only through Re_l, We_g, and Oh_m. Increasing the sheet thickness delays the hole formation and the lobe/ligament stretching process.

Different characteristic time scales were introduced for the hole formation and lobe stretching—mainly related to the surface tension and liquid viscosity, respectively. At any flow condition, the mechanism having a smaller characteristic time is the dominant process. In the transitional region, both characteristic times are of the same order; thus, both mechanisms occur simultaneously and the cascade of liquid structures varies locally. The two characteristic times are related to each other by the modified Ohnersorge number, which involves the gas Weber number and the liquid Reynolds number.

[1]E.-S. R. Negeed, S. Hidaka, M. Kohno, and Y. Takata, "Experimental and analytical investigation of liquid sheet breakup characteristics," Int. J. Heat Fluid Flow **32**(1), 95–106 (2011).
[2]B. E. Stapper, W. A. Sowa, and G. S. Samuelsen, "An experimental study of the effects of liquid properties on the breakup of a two-dimensional liquid sheet," J. Eng. Gas Turbines Power **114**(1), 39–45 (1992).
[3]H. B. Squire, "Investigation of the instability of a moving liquid film," Br. J. Appl. Phys. **4**(6), 167–169 (1953).

[4]W. W. Hagerty and J. F. Shea, "A study of the stability of plane fluid sheets," J. Appl. Mech. **22**(3), 509–514 (1955).
[5]R. H. Rangel and W. A. Sirignano, "The linear and nonlinear shear instability of a fluid sheet," Phys. Fluids A **3**(10), 2392–2400 (1991).
[6]T. J. Tharakan, K. Ramamurthi, and M. Balakrishnan, "Nonlinear breakup of thin liquid sheets," Acta Mech. **156**(1-2), 29–46 (2002).
[7]R. D. Reitz and F. V. Bracco, "Mechanisms of breakup of round liquid jets," in *Encyclopedia of Fluid Mechanics* (Gulf Publishing Co., 1986), Vol. 3, pp. 233–249.
[8]W. V. Ohnesorge, "Die bildung von tropfen an düsen und die auflösung flüssiger strahlen," J. Appl. Math. Mech./Z. Angew. Math. Mech. **16**(6), 355–358 (1936).
[9]R. P. Fraser, P. Eisenklam, N. Dombrowski, and D. Hasson, "Drop formation from rapidly moving liquid sheets," AIChE J. **8**(5), 672–680 (1962).
[10]A. Lozano and F. Barreras, "Experimental study of the gas flow in an air-blasted liquid sheet," Exp. Fluids **31**(4), 367–376 (2001).
[11]J. Park, K. Y. Huh, X. Li, and M. Renksizbulut, "Experimental investigation on cellular breakup of a planar liquid sheet from an air-blast nozzle," Phys. Fluids **16**(3), 625–632 (2004).
[12]S. Wahono, D. Honnery, J. Soria, and J. Ghojel, "High-speed visualisation of primary break-up of an annular liquid sheet," Exp. Fluids **44**(3), 451–459 (2008).
[13]J. W. Hoyt and J. J. Taylor, "Waves on water jets," J. Fluid Mech. **83**(1), 119–127 (1977).
[14]P. Marmottant and E. Villermaux, "On spray formation," J. Fluid Mech. **498**, 73–111 (2004).
[15]A. Lozano, A. Garcıa-Olivares, and C. Dopazo, "The instability growth leading to a liquid sheet breakup," Phys. Fluids **10**(9), 2188–2197 (1998).
[16]R. Scardovelli and S. Zaleski, "Direct numerical simulation of free-surface and interfacial flow," Annu. Rev. Fluid Mech. **31**(1), 567–603 (1999).
[17]O. Desjardins and H. Pitsch, "Detailed numerical investigation of turbulent atomization of liquid jets," Atomization Sprays **20**(4), 311–336 (2010).
[18]J. Shinjo and A. Umemura, "Simulation of liquid jet primary breakup: Dynamics of ligament and droplet formation," Int. J. Multiphase Flow **36**(7), 513–532 (2010).
[19]M. Herrmann, "On simulating primary atomization using the refined level set grid method," Atomization Sprays **21**(4), 283–301 (2011).
[20]D. Jarrahbashi and W. A. Sirignano, "Vorticity dynamics for transient high-pressure liquid injection," Phys. Fluids **26**(10), 101304 (2014).
[21]D. Jarrahbashi, W. A. Sirignano, P. P. Popov, and F. Hussain, "Early spray development at high gas density: Hole, ligament and bridge formations," J. Fluid Mech. **792**, 186–231 (2016).
[22]A. Zandian, W. A. Sirignano, and F. Hussain, "Three-dimensional liquid sheet breakup: Vorticity dynamics," in *54th AIAA Aerospace Sciences Meeting* (American Institute of Aeronautics and Astronautics, 2016), p. 1593.
[23]H. Zhao, T. Chan, B. Merriman, and S. Osher, "A variational level set approach to multiphase motion," J. Comput. Phys. **127**(1), 179–195 (1996).
[24]M. Sussman, E. Fatemi, P. Smereka, and S. Osher, "An improved level set method for incompressible two-phase flows," Comput. Fluids **27**(5), 663–680 (1998).
[25]S. Osher and R. P. Fedkiw, "Level set methods: An overview and some recent results," J. Comput. Phys. **169**(2), 463–502 (2001).
[26]C. W. Hirt and B. D. Nichols, "Volume of fluid (VOF) method for the dynamics of free boundaries," J. Comput. Phys. **39**(1), 201–225 (1981).
[27]W. J. Rider and D. B. Kothe, "Reconstructing volume tracking," J. Comput. Phys. **141**(2), 112–152 (1998).
[28]S. Dabiri, W. A. Sirignano, and D. D. Joseph, "Cavitation in an orifice flow," Phys. Fluids **19**(7), 072112 (2007).
[29]A. Zandian, W. A. Sirignano, and F. Hussain, "Explanation of liquid-jet atomization cascades via vortex dynamics," e-print arXiv:1706.03742 (2017).
[30]A. K. M. F. Hussain, "Coherent structures and turbulence," J. Fluid Mech. **173**, 303–356 (1986).
[31]L. P. Bernal and A. Roshko, "Streamwise vortex structure in plane mixing layers," J. Fluid Mech. **170**, 499–525 (1986).
[32]J. C. Lasheras and H. Choi, "Three-dimensional instability of a plane free shear layer: An experimental study of the formation and evolution of streamwise vortices," J. Fluid Mech. **189**, 53–86 (1988).
[33]D. Liepmann and M. Gharib, "The role of streamwise vorticity in the near-field entrainment of round jets," J. Fluid Mech. **245**, 643–668 (1992).
[34]D. G. Schowalter, C. W. Van Atta, and J. C. Lasheras, "Baroclinic generation of streamwise vorticity in a stratified shear layer," Meccanica **29**(4), 361–371 (1994).